Charge transfer reactions between rare gas ions and polar molecules



Andriana Tsikritea
Somerville College
University of Oxford

A thesis submitted for the degree of
Doctor of Philosophy
September 2021

Abstract

Charge transfer reactions between rare gas Xe^+, Kr^+ or Ar^+ ions and polar molecules are investigated. The reactions are undertaken within the cold and controlled environment of Ca^+ Coulomb crystals at temperatures lower than 300 K, spanning 194–260 K. Both fully hydrogenated and fully deuterated ammonia and water reactants are employed, with all of these neutral species known to be present in interstellar environments.

Inverse kinetic isotope effects (KIEs) are reported for the ammonia charge transfer reactions, with the deuterated molecules reacting at a faster rate than the hydrogenated species. The magnitude of the effect depends on the identity of the rare gas species; the strongest effect is observed for the Xe^+ ions. Capture theory models, which are frequently used to describe ion-molecule interactions, fail to predict these findings. Further, the experimentally measured rate coefficients are suppressed in comparison to classical and quantum capture theory predictions, indicating that the reactions are not capture limited. With the aid of high-level *ab initio* calculations, a tentative explanation is proposed, suggesting that properties of the reaction complex (such as its lifetime) may give rise to the observed inverse KIEs.

No inverse KIE—indeed, no isotope effects at all—are observed for the water charge transfer reactions, with the measured reaction rate coefficients being in good agreement with capture theory models.

As this thesis will discuss, capture theory models do not always successfully predict the behaviour of ion-molecule reactions. In the absence of experimental data, capture theory models are often employed in astrochemical databases to predict the behaviour of ion-molecule reactions. This work highlights the assumptions underpinning the widespread use of capture theories in astrochemical modelling, and proposes that there is a need for further work to establish when capture theory models can be reliably used to predict the behaviour of ion-molecule reactions.

Declaration

Parts of Chapter 3 and 4 have been published in the following papers.

L. S. Petralia*, A. Tsikritea*, J. Loreau, T. P. Softley, and B. R. Heazlewood. "Strong inverse kinetic isotope effect observed in ammonia charge exchange reactions", *Nat. Commun.*, **11**, 1, 2020.

A. Tsikritea, K. Park, P. Bertier, J. Loreau, T. P. Softley, and B. R. Heazlewood. "Inverse kinetic isotope effects in the charge transfer reactions of ammonia with rare gas ions", *Chem. Sci.*, **12**, 10005, 2021.

Parts of Chapter 5 will be published in the following paper.

A. Tsikritea, J. A. Diprose, J. Loreau, and B. R. Heazlewood. "Charge transfer reactions between water isotopologues and Kr^+ ions", 2021 (Submitted).

A fourth paper has been accepted for publication (see below for details). The manuscript does not form part of this thesis.

O. Mohamed*, L. Y. Wu*, A. Tsikritea, B. R. Heazlewood. "Optimising the intensity and purity of a Zeeman-decelerated beam", *Rev. Sci. Instrum.*, **92**, 093201, 2021.

Acknowledgements

I would like to thank the people who supported me throughout my DPhil years and contributed to the fulfilment of this work.

To Brianna Heazlewood, first and foremost, for being such a supportive and patient supervisor. Her guidance and insightfulness has inspired me and will keep doing so.
To Lorenzo Petralia, for teaching me every trick in the lab and joining me for coffee breaks in the park.
To Jutta Toscano, for her wise advice.
To Tim Softley, for all the insightful discussions.
To Michal Hejduk, for his humorous remarks. To Paul Bertier, Kibum Park and Jake Diprose, for making lab work fun. To Chloé Miossec and Kathy Wu, for their everyday enthusiasm. To all current and previous members of the Heazlewood group, who made every day enjoyable.
To the PTCL facilities team, for their tireless help throughout the years.
To all members of the PTCL mechanical and electronic workshops, for their cheerful assistance when fixing anything broken.

To my friends in Oxford, for making these four years fun.
To my friends, Konstantina Rousia, Marialena Tsirogianni and Stefanos Proimakis, for putting up with me.
To my parents, Anastasia Nikolaidou and Giannis Tsikriteas, and siblings, Valia Tsikritea and Petros Tsikriteas, for all their love. I admire each of them deeply.
To Alessandro Geraldini, who, to this date, says he is still ερωτευμένος.

I am grateful to the Clarendon foundation and Somerville College for providing me with a scholarship. Also, I would like to express my gratitude to the Onassis Foundation for their financial support (Scholarship ID: F ZP 055-1/2019-2020).

Contents

1 Introduction **1**
- 1.1 Ion-molecule interactions . . . 1
- 1.2 Ion-molecule reactions and astrochemistry . . . 4
- 1.3 Reaction studies at temperatures lower than 300 K . . . 6
  - 1.3.1 Flow techniques . . . 6
  - 1.3.2 Ion trapping . . . 7
  - 1.3.3 Merged beams . . . 15
  - 1.3.4 Future prospects . . . 16
- 1.4 Aims . . . 17

2 Ion trapping and cooling **19**
- 2.1 Ion trapping . . . 19
- 2.2 Laser cooling . . . 22
- 2.3 Coulomb crystals . . . 24
  - 2.3.1 Sympathetic cooling . . . 26
- 2.4 Experimental apparatus . . . 27

3 Ammonia charge transfer reactions **31**
- 3.1 Experimental procedure . . . 31
- 3.2 Charge transfer reactions as a one-to-one processes . . . 34
  - 3.2.1 Treatment of background reactions . . . 34
  - 3.2.2 Competitive reaction pathways . . . 36
  - 3.2.3 Trapping efficiency . . . 38
- 3.3 MD simulations . . . 39
- 3.4 Reaction rate coefficients . . . 43
  - 3.4.1 Reaction temperature . . . 47

4 Capture theories and inverse KIEs **49**
- 4.1 Capture theories . . . 49
- 4.2 Experimental results . . . 51
- 4.3 Theoretical work . . . 57
  - 4.3.1 *Ab initio* calculations . . . 58
  - 4.3.2 QM model . . . 60
- 4.4 Proposed explanation . . . 61

4.5 Implications 66

5 Water charge transfer reactions **69**
5.1 Experimental details 69
5.2 Results 72
5.3 Implications 75

6 Conclusions **79**

A ACCSA rate coefficients **83**

Bibliography **86**

Chapter 1

Introduction

1.1 Ion-molecule interactions

The interaction between ions and neutral molecules is dominated by the strong ion-dipole (or induced dipole) attractive forces at long range. Once in close proximity, reactants are expected to fall into a deep well, forming a reaction complex. This is in contrast to the traditional Arrhenius behaviour of thermally activated reactions that need to surpass an energy barrier before proceeding to products. Ion-molecule reactions are usually barrierless processes. Trapped within the well, the reaction complex can either proceed to product formation or dissociate back to reactants. Figure 1.1 illustrates a schematic of the reaction co-ordinate for a typical barrierless process. Many ion-molecule reactions have been found to exhibit a negative trend with temperature, with enhanced rates at low temperatures [1, 2].

Capture theories have been developed to describe interactions where a strong attraction governs the long-range part of the potential. The main assumption underlying capture theory models is that the rate-determining step of a reaction is the capture of the reactants and the formation of a reaction complex, after which products are formed with unit probability. The relative orbital motion of the colliding species can, however, add an effective barrier to the (otherwise barrierless) potential, giving rise

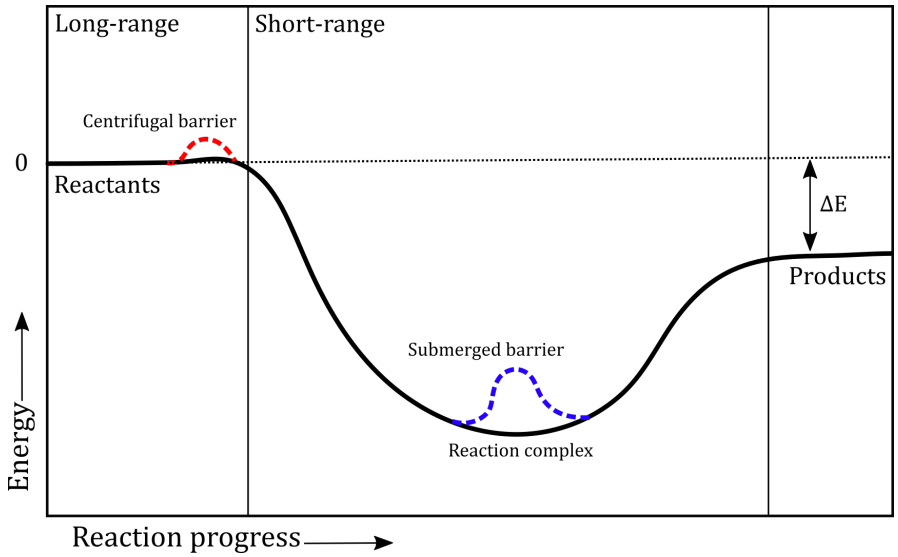


Figure 1.1: Schematic depiction of a barrierless, exothermic reaction between an ion and a neutral species. The reaction co-ordinate is divided in long-range, short-range and product sections. The strong attraction at long range depends on the distance, r, between the colliding particles (i.e., $-1/r^n$, with $n = 2$ for ion-dipole and $n = 4$ for ion-induced dipole collisions). Reactants need to surpass a centrifugal barrier at long range before forming a reaction complex at short range. The presence of a submerged barrier in some ion-molecule reaction systems can lower the probability of product formation.

to a so-called centrifugal barrier. Collision events will successfully lead to product formation only when the reactants have enough energy to surmount the centrifugal barrier. Capture theory models do not take into account short-range interactions. As such, they predict the likelihood of a reaction occurring—giving overall rate coefficients for a selected reaction system, irrespective of the possible product channels that might be available. Capture theories cannot identify or predict the branching ratios of different reaction pathways.

The simplest of capture theories, Langevin theory, is a classical model that describes the interaction between ions and non-polar molecules. It predicts no temperature

dependence for ion-neutral rate coefficients [3, 4]. Other classical capture theory models have been proposed to include the effects of temperature, polarisability, dipole moment and orientation of the reactants. For example, the average dipole orientation (ADO) theory [5] or the empirical model developed by Su & Chesnavich (SC) [6] are two commonly used capture theory models for reactions between ions and polar neutral molecules. More advanced quantum capture theories, that take into account contributions of individual rotational states to the likelihood of reaction, have also been developed. Examples of quantum capture theories include the rotationally adiabatic capture theory proposed by D. C. Clary [1, 7] and the statistical adiabatic channel model developed by J. Troe [8].

Capture theories have been found to successfully predict a number of experimentally measured rate coefficients over a temperature range that spans from $> 300\,\mathrm{K}$ down to $10\,\mathrm{K}$ [9]. However, it has also been found that submerged barriers (or other intrinsic features) on the short-range part of the potential can lead to suppression of a reaction, with products not necessarily formed after complex formation [10]. Note that even in these cases, ion-molecule reactions are usually relatively fast ($k > 10^{-11}\,\mathrm{cm^3\,s^{-1}}$) [1].

This thesis examines the success of capture theory models in predicting the rate coefficients for several ion-molecule charge transfer reactions. Chapter 4 describes in detail the calculation of classical (ADO) and quantum (ACCSA, adiabatic capture centrifugal sudden approximation) capture theory rate coefficients. A brief derivation of the ACCSA model is provided in Appendix A. The appropriateness of using capture theory calculations to predict the reactivity of a given system of interest is discussed throughout the thesis. In some reaction systems, capture theory calcula-

tions are found to successfully predict the rate of reaction. In other systems, the reaction mechanism is not capture limited and therefore capture theory predictions do not agree with experimental measurements. As this work will discuss, further work is needed to establish when capture theory models can be reliably used to predict reactivity in systems that are yet to be experimentally examined.

1.2 Ion-molecule reactions and astrochemistry

More than 200 molecular species have now been unambiguously identified in the interstellar medium (ISM) [11]. Hundreds of deuterated analogues of these molecules have also been observed [12]. In the extreme conditions prevalent in the ISM, with temperatures spanning 10–100 K, low densities, long timescales, and the presence of ionising ultraviolet radiation, barrierless ion-molecule reactions play an important role. Indeed, as the rate coefficients for many ion-molecule reaction systems increase as temperature decreases, these reactions are responsible for much of the gas-phase chemistry occurring in the lowest temperature regions of the ISM. (Other reaction processes that occur in interstellar environments, such as radiative association reactions, reactions involving radical species or reactions occurring on the surface of dust grains [13, 14], are beyond the scope of this thesis.)

Spectroscopic observations of the ISM composition, although vital, cannot alone establish how molecular species are formed. To unravel the complex chemistry that occurs in the ISM, a collaborative effort is needed—combining laboratory studies and the development of detailed models. A number of astrochemical databases have been developed that include reaction rate coefficients and branching ratios for many thousands of astrochemically relevant processes. Some widely adopted examples

include the Kinetic Database for Astrochemistry (KIDA) [15], the Meudon model for atomic and molecular interstellar gas (known as the Meudon photon-dominated region, PDR, code) [16] and the UMIST Database for Astrochemistry (UDfA) [17]. Given the ongoing challenges related to the realisation of experimental studies at low temperatures (discussed in more detail below), only a small fraction of these processes have been experimentally examined at collision energies below 300 K. As such, astrochemical databases are necessarily reliant on predictions. For ion-neutral collisions, for example, rate coefficients are often extrapolated from measurements taken at room temperature or are entirely derived from capture theory calculations [18].

A further lack of experimental data is evident when considering deuterated reactants, with very few experimental studies having explicitly considered the reactivity of deuterated species [19, 20]. Deuterium-containing molecules have been found to account for as much as 10% of the total abundance of some molecular species in regions of the ISM, a phenomenon known as deuterium fractionation. This is a striking number considering the cosmic ratio of D/H is $\approx 1.5 \times 10^{-5}$ [21]. Existing interstellar models cannot fully account for these observations, highlighting the need for further experimental studies on both hydrogenated and deuterated reaction systems.

1.3 Reaction studies at temperatures lower than 300 K

1.3.1 Flow techniques

Numerous ion-molecule reactions have been studied experimentally at 300 K utilising the flowing afterglow technique [22] and its successor, the selected ion flow tube (SIFT) technique [23, 24]. Due to the challenges associated with studying reactions with these methods, only a few experimental studies have been conducted at temperatures lower than 300 K using these techniques. For example, a variable-temperature SIFT apparatus has been used to study ion-molecule reactions at temperatures down to 205 K, however, condensation of the reactants on the cold surfaces of the apparatus hindered the study of reactions at lower temperatures [25]. Another variable-temperature SIFT apparatus has recently been developed, allowing the study of several ion-molecule reactions over a large temperature range, spanning 100–600 K. However, as approximately 0.7 mbar of buffer gas is present in the chamber throughout the reaction process, the possibility of collisions affecting the ion-molecule rate coefficients needs to be considered. Also, at least in some cases, the generation of products could not be explicitly monitored [26].

Ion-molecule reactions can be studied over a much wider range of temperatures utilising the versatile CRESU technique (Cinétique de Réaction en Ecoulement Supersonique Uniforme—reaction kinetics in uniform supersonic flow) [27, 28]. Reactant species (or their precursors) are supersonically expanded through a Laval nozzle, consisting of a convergent section followed by a divergent section (Figure 1.2). The expansion generates a uniform beam at thermal equilibrium, with both reactant

species present in a single beam. Reactions are monitored downstream. A variety of ion-molecule reactions have been investigated under conditions of true thermal equilibrium utilising the CRESU technique, at temperatures spanning 300 K down to 8 K [2, 29, 30]. Variations of the technique have been developed to allow for the mass selection of the ionic reactants (CRESUS apparatus) [31] or the pulsed injection of the reactant species in the flow [32].

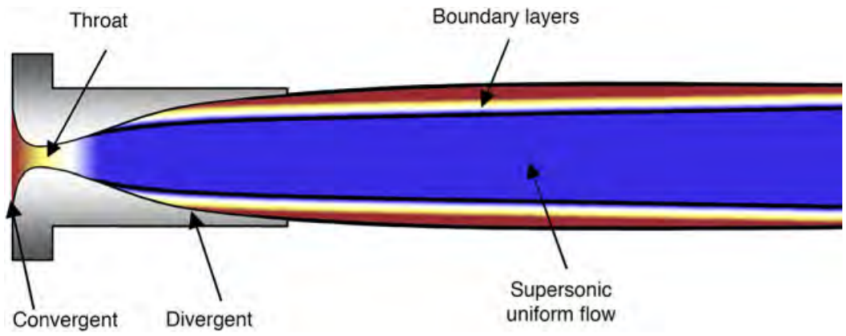


Figure 1.2: Schematic illustration of the convergent-divergent Laval nozzle used to produce uniform supersonic flows for reaction studies. (Figure reproduced with permission from Ref. [28], RSC.)

1.3.2 Ion trapping

A caveat of flow techniques is that, due to the finite length of the flow tube, only relatively fast reactions can be investigated (with rate coefficients above $10^{-12}\,\mathrm{cm^3\,s^{-1}}$ [28]). Trapping techniques, on the contrary, allow the study of slow processes, as high trapping depths result in long storage times and do not impose physical limitations (as seen in the length of the flow tube or uniform flow conditions).

Numerous reaction studies have been undertaken at 300 K using ion cyclotron resonance (ICR) cells—designed to confine ionic species within the volume of trapping

plates with the application of electromagnetic fields [33, 34]. Apart from ICR experiments, ion-molecule reaction studies have been investigated at temperatures lower than 300 K utilising radiofrequency (RF) traps. For example, a cryogenically cooled 22-pole ion trap has been used to undertake multiple reactions between trapped, buffer gas-cooled ions and neutral species at temperatures down to 10 K [35]. One such study has examined the astrochemically interesting $CH^+ + H$ reaction, where ions were stored in a variable-temperature ion trap and H atoms were produced in a cold, effusive beam (reaching temperatures as low as 12.2 K and 7.3 K, respectively) [36]. The advantage of using high-order RF traps, such as the 22-pole trap, is their steep effective potentials result in large, uniform trapping volumes. However, the optical and mechanical access in such traps is limited, inhibiting laser cooling and restricting the detection methods that can be employed [37].

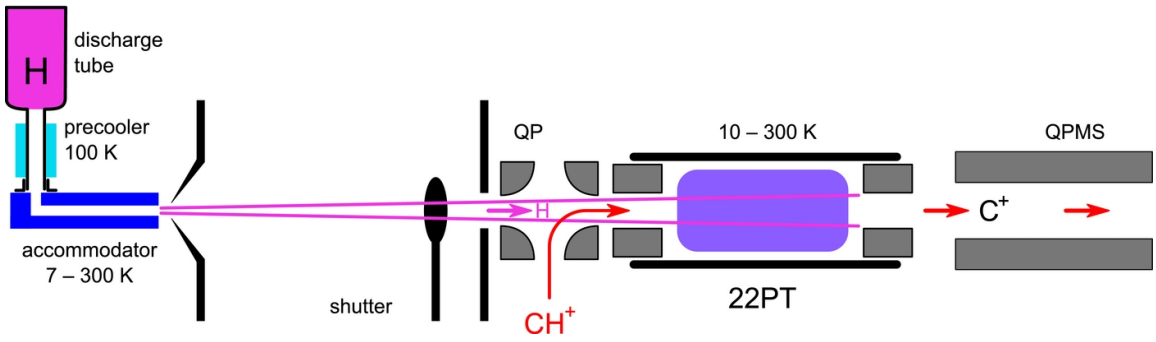


Figure 1.3: Schematic depiction of a variable-temperature 22-pole trap. (Figure reproduced with permission from Ref. [36], AAS.)

An RF octupole trap has been recently overlapped with a magneto-optical trap, aiming to investigate a variety of cold atom-ion interactions (including anionic species) [38]. The wire geometry of the trap provides the necessary optical access for future experiments with laser-cooled atoms, however, it requires the application of high

voltages for stable ion trapping.

Recently, experiments that merge ion trapping techniques with laser cooling have been realised as a powerful tool to investigate ion-molecule reactions at temperatures lower than 300 K. Trapped in linear Paul ion traps (see Chapter 2 for more details on the trap design utilised for this work), laser-cooled ionic species can form Coulomb crystals, an ensemble of ions that adopt a regular three-dimensional configuration at temperatures as low as a few mK. The ultra-high vacuum conditions under which the Coulomb crystals are formed allow for the study of reactions in an almost perturbation-free environment [39, 40]. Reactions can be studied within Coulomb crystals with great sensitivity; in many cases, the reaction of single ions can be detected [41]. Combining imaging techniques [42] and mass spectrometry detection [43] has seen the unambiguous identification of reactant and product species (as a function of time) and, therefore, the accurate measurement of reaction rate coefficients. Owing to the deep trapping potential, typically on the order of several eV, and ultra-high vacuum conditions, both slow and highly exothermic processes can be investigated. It should be noted, though, that the ionic reactants are not in thermal equilibrium, given the trapping and laser cooling forces constantly acting on them. Conventionally, a temperature can be assigned to a reaction system representing a measure of the average collision energy (in units of Kelvin). The concept of a reaction temperature, and how this is established in the systems of interest in this thesis, is discussed in more detail in Chapter 3.

Reaction studies with neutrals at 300 K

Laser-cooled ions in Coulomb crystals can undergo reactions with room-temperature neutral species admitted to the trap volume, resulting in collision temperatures on the order of 100 K. The first such reaction was reported for laser-cooled Mg^+ ions and H_2/D_2 molecules [44]. Other examples include reactive collisions between laser-cooled Be^+ ions and H_2, HD, D_2 [45], H_2O and HOD molecules [46, 47] or laser-cooled Ca^+ ions and NO [48], O_2 [49], H_2 [50] and H_2O [51]. Reactions between laser-cooled Ba^+ ions and O_2, CO_2, N_2O [52], SF_6, CH_3Cl [53] and CH_3OH [54] have also been reported. Recently, reactions between laser-cooled Ra^+ ions and CH_3OH neutrals have been undertaken [55]. However, for laser-cooled ions, a range of electronic states are populated by the cooling cycle. Hence, extracting state-specific reaction rate coefficients for the reactions of laser-cooled species is often challenging, requiring careful experimental modulation of the cooling lasers and use of the optical Bloch equations. For this reason, several processes in the above list of reaction systems do not report state-specific reactivities.

The $Be^+ + H_2O$ reaction study did succeed in measuring state-specific rate coefficients. Interestingly, the rate coefficient for ground-state Be^+ ions was found to be only half the magnitude predicted by ADO calculations. With the aid of *ab initio* calculations and the propagation of trajectories over the resulting potential energy surfaces (PESs), a submerged barrier was identified along the reaction pathway [46]. This submerged barrier was found to inhibit the formation of products, accounting for the lower-than-ADO experimental rate coefficient.

Reaction studies with sympathetically cooled ions

Laser cooling schemes cannot be implemented for the majority of atomic and molecular ions, due to the complicated nature of their energy levels. Allowing co-trapped species to be translationally cooled via elastic collisions with laser-cooled ions, a technique known as sympathetic cooling, significantly expands the pool of ions that can be used for reaction studies. (Chapter 2 outlines details of the sympathetic cooling technique.) Sympathetically cooled ions can undergo reactions with room-temperature neutrals within the framework of Coulomb crystals, resulting in reaction temperatures lower than 300 K. For example, this technique has been used to investigate the competing reaction mechanisms—probed using different isotopologues—for reactions between sympathetically cooled $C_2H_2^+$ and isomers of C_3H_4 [56, 57]. Similarly, reaction rate coefficients were measured for the astrochemically interesting $CCl^+ + C_2H_2$ [58] and $CCl^+ + CH_3CN$ reactions [59]. Capture theory predictions were in good agreement with these experimental measurements. However, a faster rate of reaction was observed for the deuterium-substituted CH_3CN reactant than the hydrogenated isotopologue, an effect that could not be accounted for by the ADO model. A similar effect is observed in the charge transfer reactions discussed in later chapters.

Reaction studies with cold neutrals

Reactions can be studied at lower temperatures when trapped ions are combined with a beam of cold (instead of 300 K) molecules. For example, a bent quadrupole guide has been used to produce velocity-selected CH_3F, CH_3Cl and CH_2F_2 neutrals that, after exiting the guide, were allowed to interact with trapped, laser-cooled

Ca^+ ions [10]. In this study, the height of a submerged barrier was again found to influence the agreement between experimental rate coefficients and capture theory predictions. Reactions between laser-cooled Ca^+ ions and velocity-selected ND_3 and CH_3CN (produced by a Stark velocity filter) have also been investigated [60]. The same set-up was used to undertake reactions between sympathetically cooled N_2H^+ and velocity-selected CH_3CN at collision energies around 3 K. The study noted the difficulty in reporting accurate reaction rate coefficients due to challenges associated with establishing the number densities of the velocity-selected species. Nevertheless, such experiments provide useful comparisons with capture theory predictions at astrochemically relevant temperatures.

In another experiment, an electrostatic deflector was used to separate the conformers of 3-aminophenol before reaction with laser-cooled Ca^+ ions [61, 62]. The reactivity of ortho- and para-H_2O with sympathetically cooled $NH_2{}^+$ was also probed with the same apparatus [63]. The different reactivity of the two H_2O molecules was successfully described within the framework of rotationally adiabatic quantum capture theory. With the exception of the two electrostatic deflector studies, in all other examples given in this subsection, the neutral reactants were not in thermal equilibrium; while the collision energy was low, the internal energy of the reactants was typically room temperature. (The electrostatic deflector studies used a pulsed valve source, giving rise to higher collision energies but very low internal energies of the neutral reactants.)

Recently, progress has been made to study processes at truly low temperatures—with low internal energy in the reactants in addition to low collision energies. Reactions between sympathetically cooled C^+ ions and buffer-gas cooled H_2O (both

species relevant to the ISM chemistry) were studied utilising the environment of Be^+ Coulomb crystals, at a reaction temperature around 20 K [64]. The use of buffer gas cooling ensured that the water reactants were vibrationally and rotationally cold, enabling the reaction to be studied under conditions directly relevant to those found in the ISM. As such, the measured reaction rate coefficients and branching ratios can be directly implemented to astrochemical models. To exert even more control over the properties of the neutral reactants, several combined experimental set-ups have been proposed. For example, a number of research groups (including the Liverpool group) are actively working towards combining an ion trap with sources of cold molecules, such as a beam of Stark decelerated polar neutrals [65] or Zeeman decelerated radicals [66, 67]. Such experiments will enable the quantum state and velocity of the neutral reactant to be precisely controlled. It is proposed that such experimental measurements will test fundamental aspects of chemical reactivity.

Linear Paul traps have been overlapped with magneto-optical traps, combining a source of cold, trapped ions with ultra-cold trapped atoms [68, 69, 70]. These so-called hybrid traps provide a means of studying ion-molecule collisions—reactive or not—at temperatures as low as a few mK. In one example, the influence of short- and long-range effects on reaction pathways was tested for the charge transfer reactions between sympathetically cooled O_2^+ or N_2^+ and ultracold Rb atoms [71].

Sympathetically cooled molecular ions do not undergo inelastic collisions with the laser-cooled ions (ion-ion distances in Coulomb crystals are typically on the order of 20 μm). Hence, although translationally cold, they typically have thermal rovibrational temperatures. Even when a cold or state-selected molecular beam is employed, ambient black-body radiation results in (comparatively) fast thermalisation

of the internal degrees of freedom, inhibiting the study of state-specific reactions (as reactions are typically studied over the course of minutes) [72]. Cryogenically cooled ion traps, such as the CryPTEx apparatus [73] and the ion trap currently under development in the Liverpool lab [74], overcome this limitation and offer the prospect of studying reactions involving trapped molecular ions under truly cold conditions. As illustrated in Figure 1.4, the Liverpool apparatus will aim to study cold, state-selected reactions by combining a cryogenic ion trap environment—with temperatures as low as 10 K—with a pure beam of Zeeman decelerated (and velocity tunable) radicals.

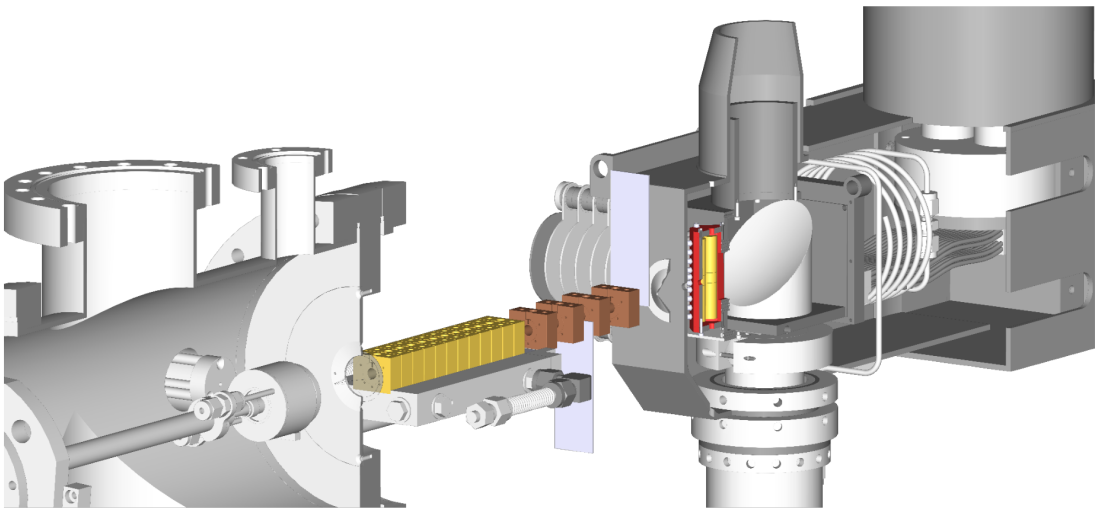


Figure 1.4: Schematic illustration of the cryogenic ion trap currently under development in the Liverpool lab. On the LHS is a pulsed valve and the 12-stage Zeeman decelerator (shown in gold), followed by a magnetic guide (in brown) and skimming blades (light blue). The Zeeman decelerator and guide are interfaced with the ion trap (shown in gold), positioned inside two nested temperature stages and attached to a pulse tube cryocooler. An off-axis parabolic mirror array provides optical access to the trap centre. (Figure produced by M. Hejduk.)

A universal drawback of reactions studies undertaken in RF traps is the RF-induced

heating experienced by the trapped ions (more details can be found in Chapter 2). To minimise the effects of heating of trapped ions, and to reach the lowest-possible collision energies, it is possible to study the reactions of strings of (or even one or two) ions. When ions are located exclusively along the null line of the trap, RF-induced micromotion effects are avoided. RF-induced heating can also be avoided when Penning traps are utilised to undertake reactions, as ions are confined by a combination of static magnetic and electric fields. For example, a helium-cooled Penning trap has been used for reaction studies, reaching temperatures as low as 10 K [75, 76]. However, the presence of a magnetic field complicates the implementation of laser cooling schemes in such apparatuses [77].

1.3.3 Merged beams

Experiments involving the merging of two beams have also been used to investigate ion-molecule reactions at temperatures lower than 300 K. A merged fast-beam apparatus has been developed to combine a molecular ionic beam with a neutral beam using an 90° electrostatic deflector. Astrochemically interesting reaction systems such as C + H_3^+ [78], C + H_2^+ or D_2^+ [79] and D + H_3^+, H_2D^+ or D_2H^+ [80] have been investigated using this apparatus. Although collision energies as low as 72 K were achieved, the internal temperature of the molecular ions was on the order of a few thousand K. Also, the technique was limited at detecting product ions that are heavier than the ionic reactant species. A Rydberg-Stark deflector has also been used to merge a Rydberg and a neutral molecular beam, allowing the reaction temperature to be adjusted from 10 K to few hundred mK. The "ionic" reactants resided in a high Rydberg state (it was assumed that the Rydberg electron does not

influence the reactions). An enhancement of the reaction rate coefficient at temperatures below 1 K was reported for the $H_2^+ + H_2$ reaction. As H_2 is non-polar, these findings are in disagreement with calculations from the Langevin capture theory model that predicts rate coefficients to be independent of temperature [81]. $He^+ + CH_3F$ reactions were also reported to have increased rate coefficients below 1 K. However, as the neutral molecule employed in this reaction was polar, the behaviour was successfully rationalised in the context of the statistical adiabatic channel model developed by J. Troe [82].

1.3.4 Future prospects

This section has attempted to provide an overview of the main techniques used to study ion-molecule reactions at collision energies lower than 300 K. Examples have been discussed and a particular focus has been given to the trapping and laser cooling techniques relevant to the charge transfer reactions detailed in this thesis. The focus has been exclusively on cationic species, as Coulomb crystal studies have been limited to cations to date. Laser cooling of anionic species is more challenging as the excess electron is weakly bound, resulting in few available bound excited states. Nevertheless, recent developments have identified potential anionic candidates where laser cooling schemes might be possible, such as La^-, Os^- [83], Ce^- [84] and even molecular C_2^- [85, 86]. Laser cooling of molecular cations is also an expanding field [87]. As noted above, the newly developed hybrid octupole trap also aims at investigating the reactivity of anionic species [38]. These developments, although very challenging to be realised experimentally, illustrate the potential future of the field; it is likely that many more classes of ion-molecule reaction systems will be

able to be experimentally investigated at low temperatures in the coming years.

1.4 Aims

The work described in this thesis concerns the study of ion-molecule reactions undertaken within the cold and controlled environment of Ca^+ Coulomb crystals, trapped in a linear Paul trap. Ground-state, sympathetically cooled rare gas ions, namely Xe^+, Kr^+ or Ar^+, undergo charge transfer reactions with thermal ammonia neutrals. Both the fully hydrogenated and fully deuterated molecules are employed. Further reaction systems are examined using water isotopologues and Kr^+ ions. Note that, as the neutral reactants are at 300 K, the effective temperature of the reactions, although lower than 300 K, is still comparatively "warm" (spanning 194–260 K).

Ammonia and water, as well as their deuterated analogues, have been detected in the ISM [88, 89]. The reactions of heavier rare gas ions are not directly relevant to astrochemistry, however, lighter rare gas ions have been observed in interstellar environments. Relevant to this work, argon is known to be present in the ISM and Ar^+ is expected to play a role in interstellar chemical reactions [90]. Rate coefficients measured for the ammonia reactions are found to be consistently suppressed in comparison to classical and quantum capture theory predictions. Additionally, inverse KIEs are observed, with the deuterated species reacting at a faster rate than the hydrogenated species. The magnitude of the effect varies with the identity of the rare gas species; the (heaviest) Xe^+ ions show the strongest effect, while the (lightest) Ar^+ ions exhibit the least pronounced inverse KIE. In combination with high-level *ab initio* calculations, a tentative explanation is given—proposing that properties of the reaction complex, such as its lifetime, could give rise to the observed effects.

Although the charge transfer reactions are undertaken at temperatures higher than those prevalent in the ISM, the observed disagreement with capture theories suggests that it is unlikely that such models will accurately predict the behaviour of the reactions at lower temperatures.

No KIE is observed for the water charge transfer reactions, and the measured rate coefficients appear to be in good agreement with capture theory models. Taken together, the experimental findings for the ammonia and water charge transfer systems illustrate that capture models do not consistently describe the behaviour of ion-molecule reaction systems.

The outline of this thesis is as follows. Chapter 2 provides a brief overview of the trapping and cooling techniques used to undertake the charge transfer reaction studies. Chapter 3 describes the ammonia reactions and details the analytical techniques used to measure reaction rate coefficients. Chapter 4 discusses the experimental results within the framework of capture theory models and attempts to propose an explanation for the observed findings. Chapter 5 reports the water charge transfer reaction findings, and attempts to explore the role that capture theories play in describing the behaviour of ion-molecule reactions in more general terms. Finally, Chapter 6 concludes the findings and sets out the basis for future work.

Chapter 2

Ion trapping and cooling

The charge transfer reactions discussed in later chapters take place within the confines of Ca^+ Coulomb crystals, where cold, co-trapped rare gas ions undergo reactive collisions with thermal ammonia or water neutrals. This chapter details the ion trapping and cooling techniques used, together with the main aspects of Coulomb crystals. A focus is given to properties relevant to the charge transfer reactions. The experimental apparatus used is also described in detail.

2.1 Ion trapping

A combination of RF and static voltages can be used to confine charged particles. Devices employing RF and static voltages in this way are known as Paul traps (named after Wolfgang Paul, whose seminal work was awarded the Nobel prize in Physics in 1989 [91]). The charge transfer reactions in this work take place in a linear Paul trap, the design of which is based on the trap developed at Aarhus University [92]. A schematic illustration is given in Figure 2.1. The trap consists of four stainless steel cylindrical rods placed in a quadruple geometry. Each rod is segmented into three parts, with Macor insulators electrically isolating each segment from the others. Alternating RF voltages of equal magnitude but opposite polarity

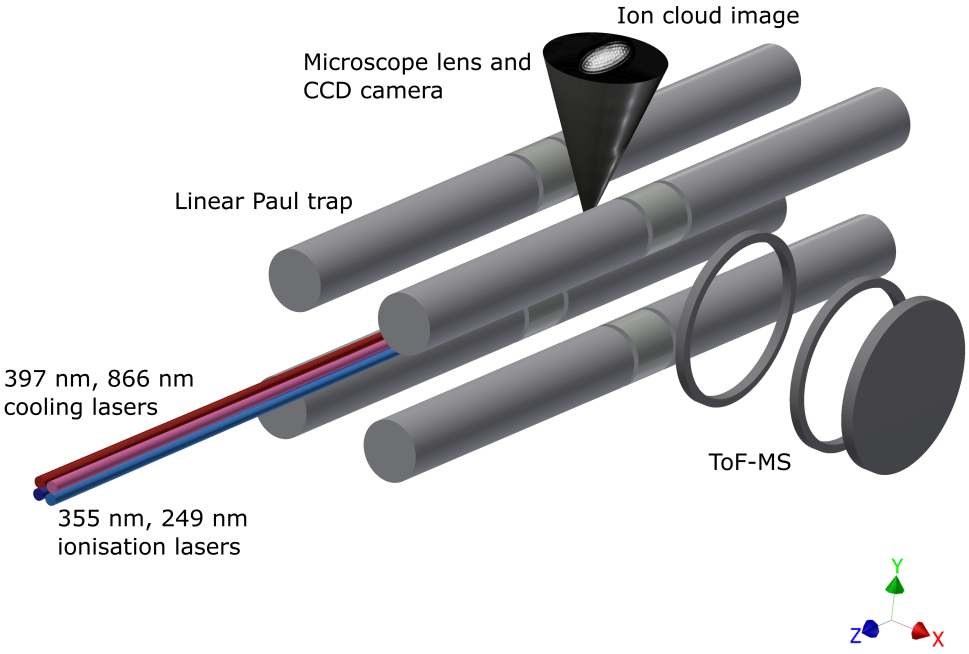


Figure 2.1: Schematic depiction of the experimental apparatus used to study the ion-molecule reactions. A combination of RF and static voltages are applied to the four rods, confining the ions. The fluorescence of the laser-cooled species is captured with a charge-coupled device (CCD) camera placed on top of the ion trap. Time-of-flight mass spectra (ToF-MS) are recorded by ejecting the ions towards a microchannel plate (MCP) detector.

are applied to each pair of diagonal rods, following the equation

$$V_{\mathrm{RF}}(t) = \pm\frac{1}{2}V_{\mathrm{RF}}cos(\Omega_{\mathrm{RF}}t). \tag{2.1}$$

V_{RF} and Ω_{RF} are the peak-to-peak voltage and the oscillating frequency ($\Omega_{\mathrm{RF}} = 2\pi f_{\mathrm{RF}}$), respectively. A rotating saddle point is created in this way, dynamically trapping the ions in the radial plane (x-y). To confine the ions in the axial direction (z), an additional static voltage is applied on the endcaps (outer segments) of each rod.

The motion of a single ion confined in a linear Paul trap can be described using a set of equations known as Mathieu equations [91]. Stable confinement of the ions depends only on the values of the two dimensionless Mathieu parameters a and q, where $a_{\mathrm{x}} = a_{\mathrm{y}} = -\frac{1}{2}a_{\mathrm{z}} = -\eta\frac{4QU_{\mathrm{end}}}{m\Omega_{\mathrm{RF}}^2 z_0^2}$ and $q_{\mathrm{x}} = -q_{\mathrm{y}} = \frac{2QV_{\mathrm{RF}}}{m\Omega_{\mathrm{RF}}^2 r_0^2}, q_{\mathrm{z}} = 0$, respectively. η is a geometric factor accounting for the non-ideal geometry of the trap, Q the charge of the ion, U_{end} the endcap voltage, m the mass of the ion, $2z_0$ the endcap separation (the length of the central electrodes) and $2r_0$ the diagonal electrode surface separation (the distance between opposite rods). The operating trapping parameters as well as the dimensions of the trap used to undertake the charge transfer reactions are summarised in Table 2.1.

Table 2.1: Operating parameters and dimensions of the linear Paul trap used in this work.

RF voltage (V_{RF})	$180 - 250$ V
RF frequency (Ω_{RF})	$2\pi \times 3.82$ MHz
DC voltage (U_{end})	$2.0 - 3.0$ V
Endcap separation ($2z_0$)	5.5 mm
Diagonal electrode surface separation ($2r_0$)	7 mm
Electrode radius (R)	4 mm
Geometric factor (η)	≈ 0.27

One can separate the motion of the trapped ions into two components, a fast periodic motion caused by the alternating RF fields, known as micromotion, and a slow secular motion [35]. The former vanishes at the trap axis and increases with the distance from it. The latter corresponds to the thermal motion of the ions assuming they experience a pseudopotential of the form

$$V^*(R_0) = \frac{Q^2 E_0^2}{4m\Omega_{\mathrm{RF}}^2} + Q\Phi_{\mathrm{end}}. \tag{2.2}$$

The first term in equation 2.2 represents a time-averaged potential resulting from the RF fields, with E_0 being the voltage amplitude. Φ_{end} in the second term represents the potential arising from the static fields. The position of the ions within the trap depends on their mass (i.e., the $1/m$ term in the pseudopotential). When different ionic species are present in the trap, lighter species experience a steeper potential and, therefore, are confined closer to the trap axis. Note that cooling techniques—either laser or sympathetic cooling—target the secular motion rather than the micromotion.

2.2 Laser cooling

Laser cooling was originally independently proposed for neutral [93] and ionic species [94], with its further experimental and theoretical development being awarded the Nobel prize in Physics in 1997 [95, 96, 97]. A brief description of the fundamental principles of laser cooling is given below.

Laser cooling relies on the continuous absorption and spontaneous emission of photons within a closed transition cycle. According to the laws of conservation of momentum, absorption of a photon changes the momentum, and therefore the velocity, of a particle. This transfer of momentum, depending on the relative movement of the photon and the particle, can either accelerate or decelerate the particle. Deceleration is achieved when the frequency of the laser beam is red-shifted, as only those particles that travel towards the beam encounter photons with the right transition frequency (due to the Doppler effect). As the spontaneous emission happens in a random direction, the particle's velocity is overall decreased after many absorption/emission cycles (usually more than 10^4 events are needed to reach temperatures

close to zero). The technique is also known as Doppler laser cooling.

Laser cooling neutral atoms requires six counter-propagating beams in three orthogonal directions. Trapped atomic ions, on the contrary, can be efficiently cooled by only one laser beam, since all translational degrees of freedom are coupled by the Coulomb interactions and trapping fields. A second counter-propagating beam can be implemented to equilibrate the forces that act on the ions or to reach the Doppler temperature limit, $T_{\min} = \frac{\hbar\Gamma}{2k_B}$. $\hbar$ is the Planck's constant, Γ is the linewidth of the cooling transition and k_B the Boltzmann constant. For the 397 nm cooling transition used in the Ca^+ laser cooling scheme, $T_{\min} = 0.5\,\text{mK}$ [98].

A simplified representation of the Ca^+ energy levels is given in Figure 2.2, showing the states relevant to the laser cooling cycle. Cooling is performed by exciting the

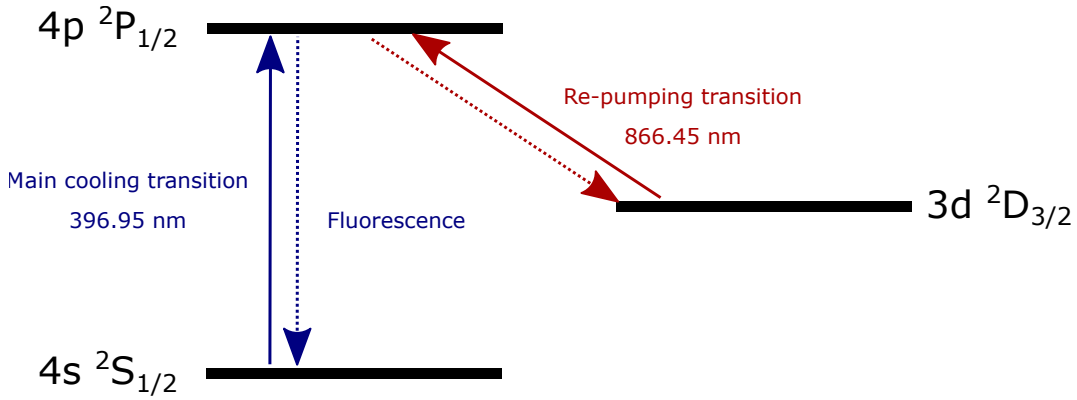


Figure 2.2: Ca^+ energy levels involved in the laser cooling scheme. The main cooling and re-pumping transitions at 397 nm and 866 nm, respectively, close the laser cooling cycle, ensuring efficient cooling of the ions.

$4s\,^2S_{1/2} \rightarrow 4p\,^2P_{1/2}$ transition at 397 nm. The $4p\,^2P_{1/2}$ state either decays to the ground $4s\,^2S_{1/2}$ state or the metastable $3d\,^2D_{3/2}$ state, with a branching ratio of approximately 12:1 [98]. For efficient laser cooling, a second laser beam at 866 nm

is introduced that re-pumps the ions from the metastable $3d\,^2D_{3/2}$ state back to the $4p\,^2P_{1/2}$ state, effectively closing the cooling cycle. Laser induced fluorescence produced during the spontaneous emission is used to monitor the presence of the Ca^+ ions in the trap (as detailed in section 2.3).

2.3 Coulomb crystals

The trapped, laser-cooled ions undergo a phase transition to a form of matter known as Coulomb crystals (originally proposed by Wigner for the arrangement of electrons in solids [99]). Coulomb crystals adopt a lattice-like structure where the ions minimise their potential energy by equilibrating the forces of the trapping fields and the Coulombic repulsion. Coulomb crystals formed in linear Paul traps with parameters similar to the ones given in Table 2.1 have an ellipsoidal structure of concentric shells.

Coulomb crystals have been described as strongly coupled non-neutral plasmas [100]. The plasma coupling parameter (i.e., the ratio of the potential energy of the ions to their kinetic energy), Λ, is given by

$$\Lambda = \frac{E_{\mathrm{pot}}}{E_{\mathrm{kin}}} = \frac{Q^2}{4\pi\varepsilon_0\alpha_{\mathrm{ws}}k_{\mathrm{B}}T}. \tag{2.3}$$

The Wigner-Seitz radius, $\alpha_{\mathrm{ws}} = \sqrt[3]{\frac{3}{4\pi n_0}}$, is a measure of the ion-ion distance, with n_0 the particle density. Coulomb crystals are formed when $\Lambda > 150$ [101, 102]. Limited by the Coulombic repulsion, the distance between neighbouring ions in Coulomb crystals is on the order of 20 μm (with number densities around 10^8 ions/cm^3) [103]. As such, following equation 2.3, Coulomb crystallisation occurs at a temperature around 100 mK.

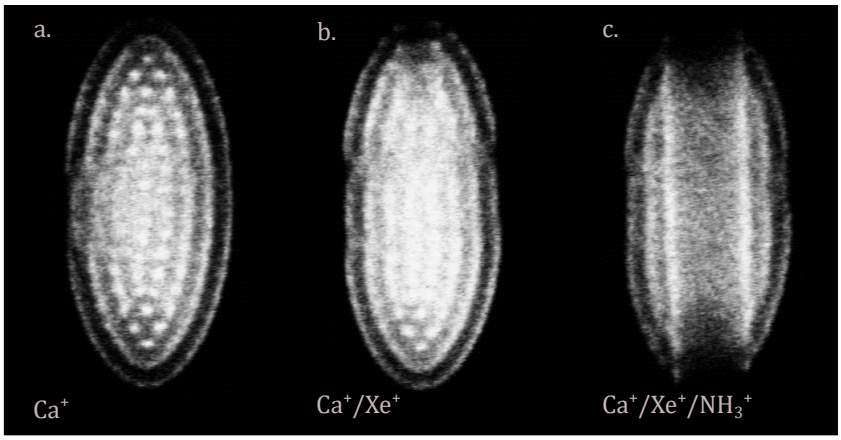


Figure 2.3: Images of Coulomb crystals taken with a CCD camera. The lattice-like structure of the crystals is evident in the Ca^+ mono-component crystal (a). Dark, sympathetically cooled ions induce changes in the shape of multi-component crystals, with heavier ions, such as Xe^+, flattening the edges of the crystal (b) and lighter species, such as $NH_3{}^+$, forming a dark core (c).

Note that the term crystal is a misnomer, considering that the average distance between the trapped species (20 μm) is much greater than the distances of common solid-state crystals. Additionally, the ions are able to diffuse through the crystal, rather than being in fixed positions. The lattice structure of the crystal represents the positions of potential energy minima, in which the ions are most likely to be found. Monitoring the laser induced fluorescence of the laser-cooled ions can reveal the location of these lattice points. An example of a Ca^+ Coulomb crystal is given in Figure 2.3a, where the ordered structure is captured with a CCD camera. The camera focus is adjusted to the central plane of the crystal, producing images of two-dimensional ellipses that represent the spheroidal structure of the crystals.

2.3.1 Sympathetic cooling

The laser-cooled Ca^+ ions do not take part in the charge transfer reactions studied in this thesis. However, they constantly remove kinetic energy from the co-trapped ionic reactants and products, a technique called sympathetic cooling. Sympathetic cooling is achieved via elastic collisions between the laser-cooled ions and other co-trapped species and results in the decrease of the translational energy of the latter. The coupling between laser- and sympathetically cooled ions, and therefore the efficiency of the cooling, is stronger when the mass-to-charge ratios of the species are similar, ideally ranging from 0.4 to 2.5 [103]. Sympathetic cooling was first reported for atomic ions (Hg^+ in laser-cooled Be^+ ions) [104] and later for a number of molecular species [105]. The internal degrees of freedom of molecular ions remain unaffected as Coulombic repulsion prevents inelastic collisions from occurring.

Considering the pseudopotential form in equation 2.2, the positions of the laser- and sympathetically cooled ions in the trap depend on their relative Q^2/m ratio. For singly charged ions, species lighter than Ca^+ concentrate closer to the trap axis (effectively pushing the Ca^+ ions outwards), whilst heavier species are confined further away (pushing the Ca^+ inwards). The sympathetically cooled ions, as no laser is acting directly on them, do not fluoresce. Hence, they appear in the Coulomb crystal images as dark regions. Their presence is inferred from the change they induce in the positions of the Ca^+ ions. As illustrated in Figure 2.3b and c, heavier and lighter ions form a dark outer shell and a dark core, respectively. Reactions between sympathetically cooled ions and molecular species can be monitored by the changes in the structure of the Ca^+ Coulomb crystal images (Chapter 3 describes in detail how this method is adopted for the study of charge transfer reactions).

2.4 Experimental apparatus

Figure 2.4 illustrates a top-view schematic of the experimental apparatus used to study the charge transfer reactions. The ion trap is mounted in the centre of a cylindrical reaction chamber, where ultra-high vacuum conditions are achieved with a scroll pump-backed turbomolecular pump (Leybold Turbovac 361). The pressure in the reaction region is measured using a Bayard-Alpert ion gauge (Arun Microelectronics LTD). A baseline pressure of $\approx 1.0 \times 10^{-9}$ mbar is reached after baking the chamber at 180 °C for 5–10 days (a procedure necessary after venting or opening the chamber). A heat exchange device, placed in close proximity to the ion trap, serves to freeze out any remaining gaseous contaminant species present in the reaction chamber. Liquid-nitrogen-cooled N_2 gas passes through a series of turns of tubing, resulting in the freezing out of contaminants. Additionally, a residual gas analyser device (RGA, Stanford Research Systems 100) can be used for the identification of any contaminant gases present in the ion trap volume.

Ca atoms are produced by a resistively heated oven (AlfaSource Calcium 225 mg, purity 99.8%) at 600–900 K with the application of an 8 A current. The produced effusive beam of atomic Ca passes through a 1 mm slit skimmer, to reduce the divergence of the beam and minimise the deposition of calcium on the trap rods. A mechanical shutter allows the beam to reach the ion trap only during the loading procedure. Ca atoms are subsequently non-resonantly ionised at the trap centre with a 355 nm laser beam (the frequency-tripled output of a pulsed Nd:YAG laser, 5 ns pulses at a 10 Hz repetition rate). The ionisation laser beam, as well as all other laser beams, enters the chamber through a Brewster window and passes through an iris before reaching the trap, reducing stray light reflections.

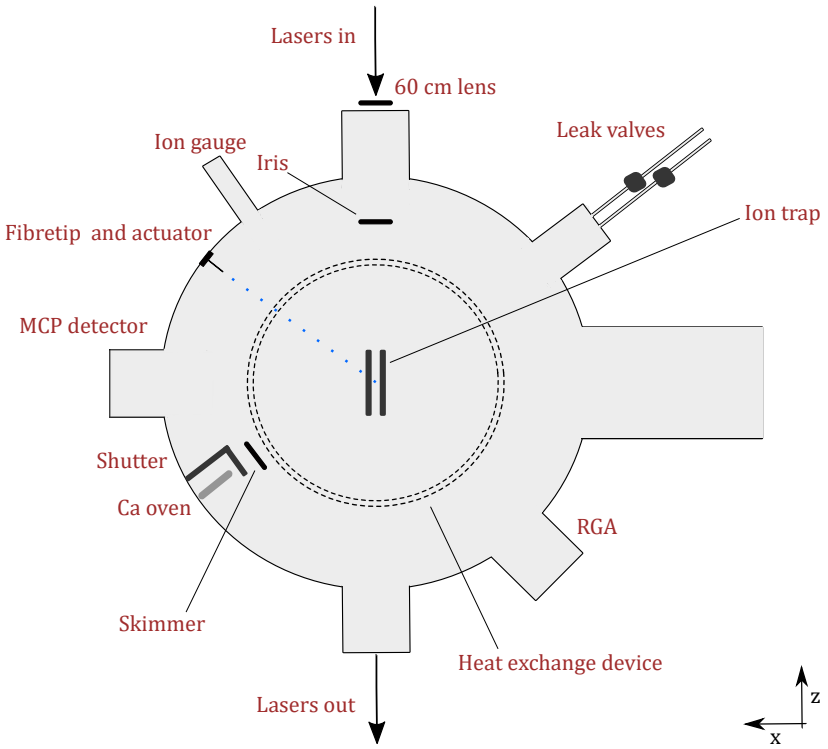


Figure 2.4: Schematic illustration of the experimental chamber used to study reactions. The linear Paul trap lies in the centre of the chamber. The heat exchange device and the CCD camera (not shown) are placed in the perpendicular plane above the ion trap.

Two continuous wave diode lasers at 397 nm (main cooling transition, Toptica DL 100 Pro) and 866 nm (re-pumping transition, Toptica DL 100) are used for laser cooling Ca^+ ions. A 60 cm lens placed at the entrance of the chamber focuses the beams beyond the trap centre, which lies at around 30 cm from the viewport. A wavemeter—interfaced with both diode lasers—allows the tuning of the diodes to coincide with the relevant transition frequencies (HighFinesse WS-8). Ca^+ Coulomb crystals can remain trapped without any ion loss for tens of minutes, a timescale more than sufficient for studying reactions. Two high-precision leak valves (Kurt J.

Lesker, Manual SS All-Metal Leak Valves) are used to introduce atomic or molecular neutrals in the trap volume.

A CCD camera and a 10× microscope objective lens are placed on top of the ion trap chamber, perpendicular to the trap axis. Imaging the Ca^+ ions' laser induced fluorescence is possible through a quartz view port. Both the camera and the microscope lens are mounted on a *x*-*y*-*z* translational stage, allowing the alignment of the camera to the trap centre. A small optical fibre tip, which can be placed in the geometric centre of the trap by a mechanical actuator, is used to align the lasers and imaging system.

Finally, a flight tube and a MCP detector are located perpendicular to the trap axis, allowing the detection of ions through time-of-flight mass spectrometry [43]. As shown in Figure 2.5, the trapping fields are switched off and two static voltages are applied to the trap rods, forming a repeller-extractor pair (at 305 V and 176 V, respectively). Ions are ejected towards the flight tube ($\approx$ 12.4 cm) and the MCP detector. To avoid interference of the residual RF voltage on the static pulse, a delay of 1.26 μs is introduced to allow the damping of the RF fields prior to the ejection pulse. It should be noted that the technique, although valuable for the unambiguous identifications of dark ions present in the Coulomb crystals, is destructive; a number of repeat measurements are required for each set of experimental conditions.

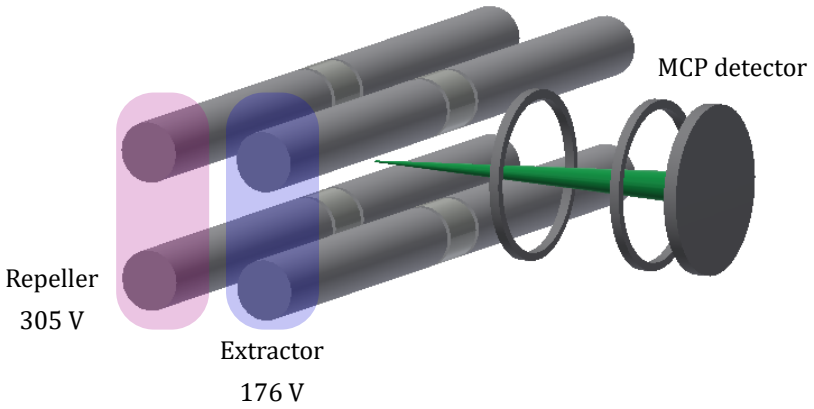


Figure 2.5: Two static voltages are applied to the trap rods forming a repeller-extractor pair, ejecting the ions from the trap towards a flight tube and an MCP detector (note that the different elements of the apparatus are not drawn to scale).

Chapter 3

Ammonia charge transfer reactions

The six ammonia systems studied are electron transfer reactions between fully hydrogenated or fully deuterated ammonia neutrals (NH_3 or ND_3) and ground-state rare gas ions (Rg^+: Xe^+, Kr^+ or Ar^+).

$$Rg^+(^2P_{3/2}) + NH_3(^1A_1) \longrightarrow Rg + NH_3{}^+(^2A_2'')$$

This chapter outlines the details of the experimental procedures followed to undertake the charge transfer reactions as well as the methods used to calculate reaction rate coefficients. The reactions are evaluated as one-to-one processes and any contributions from competitive reaction channels are discussed. With the aid of molecular dynamics (MD) simulations, the Coulomb crystal images are analysed and the results are fit to a pseudo-first order kinetic model to extract reaction rate coefficients.

3.1 Experimental procedure

Cold and stable Ca^+ Coulomb crystals need to be obtained before the reactant species are introduced in the ion trap volume. Using a crystal as a probe, the cooling lasers are aligned to obtain a well-defined and sharp lattice structure. The ellipsoidal symmetry of the crystals can be compromised by small stray fields perturbing the harmonic potential of the trap. By adjusting the bias static voltages, the ions

are directed to a position where their symmetry is optimal. An iteration of this optimisation is frequently necessary during the course of data collection, as the crystals are sensitive to the laboratory and trap conditions.

Rare gas atoms enter the ion trap volume through a high-precision leak valve and are subsequently ionised at the centre of the trap via appropriate resonance enhanced multi-photon ionisation (REMPI) schemes. Xe^+ ions are produced by a (2+1) REMPI process at 249.6 nm, using the doubled output of a 355 nm Nd:YAG-pumped dye laser (0.4 mJ/pulse, measured at the entrance of the reaction chamber). A (2+1) REMPI scheme at 212.2 nm, from the tripled output of a 532 nm Nd:YAG-pumped dye laser (0.13 mJ/pulse), is used for the ionisation of the Kr atoms, whilst Ar^+ ions are produced by a (3+1) REMPI beam at 314.5 nm, from the doubled output of a 532 nm Nd:YAG-pumped dye laser (10 mJ/pulse). Efficient sympathetic cooling of the ions is achieved during a delay of 30–60 sec that is introduced at this stage. This delay also ensures that all rare gas ions are in their ground $^2P_{3/2}$ state. Approximately 22% of Xe^+ ions are formed in the higher-energy $^2P_{1/2}$ spin state [106]. Although the $^2P_{1/2} \rightarrow {}^2P_{3/2}$ transition is electric dipole forbidden, the magnetic dipole transition is allowed with an Einstein coefficient of $A_m = 21\,s^{-1}$, resulting in an upper state lifetime of approximately 48 ms [107]. As such, the delay allows the Xe^+ ions to decay to the energetically lower-lying $^2P_{3/2}$ spin state prior to undergoing reactions with ammonia. Similarly, a subset of Kr^+ ions are produced in the higher energy $^2P_{1/2}$ spin state. They are allowed to decay to the ground state via the magnetic dipole transition with an Einstein coefficient of $A_m = 2.8\,s^{-1}$ and an approximate upper state lifetime of 340 ms. For the Ar^+ ions, the implemented (3+1) REMPI scheme results in a $97 \pm 3\%$ ground-state population [108], however

a 30 s delay is again introduced to allow for the sympathetic cooling of the ions.

A reaction is initiated when room-temperature neutrals are admitted to the ion trap via a second high-precision leak valve. To establish the partial pressure of the reactant molecules, the pressure in the reaction region is measured using a Bayard-Alpert ion gauge, calibrated to the residual gas analyser. Systematic uncertainties in pressure gauge readings are difficult to quantify and are not included in reported uncertainties [49, 64]. This systematic uncertainty does not affect the relative reaction rate coefficients recorded for each reaction system, as the same methodology and ion gauge is used for each set of experimental measurements. Note, however, that such additional systematic uncertainties should be considered when comparing the rate coefficients to measurements undertaken using different techniques.

The reaction progress is monitored by recording Coulomb crystal images at time intervals of approximately 2 s. Figure 3.1 illustrates a sequence of such images captured at different times during a charge transfer reaction between Xe^+ and NH_3. The formation and growth of a dark core indicates the formation of products (ammonia ions). Once the reaction is complete, the crystal is ejected towards the flight tube and MCP detector. The absence of a rare gas ion peak in the recorded ToF trace confirms the completion of the reaction (see, for example, Figure 3.2). For each reaction system studied, tens of repeat measurements are undertaken exploring a variety of parameters such as the Coulomb crystal size (typically ranging between 150–600 Ca^+ ions) and the partial pressure of the ammonia neutrals (varied between 1×10^{-9} and 5×10^{-9} mbar). Before moving to a different isotopologue, the reaction chamber is baked at a temperature of 50 °C to ensure that any remnant ammonia neutrals are removed.

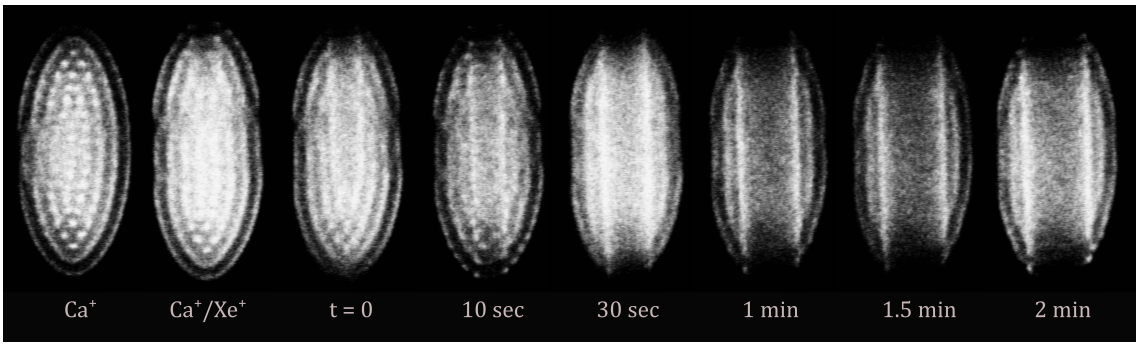


Figure 3.1: Coulomb crystal images at different times during a charge transfer reaction between Xe^+ ions and NH_3 neutrals. At $t = 0$, ammonia is introduced to the ion trap volume, initiating the reaction. The formation and growth of a dark core qualitatively shows the reaction progress.

3.2 Charge transfer reactions as a one-to-one processes

3.2.1 Treatment of background reactions

It is essential that any contaminants—and competing reaction processes—are eliminated (or at least minimised and quantified) before the reactions of interest are quantitatively studied. Any gaseous contaminants present in the chamber can be identified using the residual gas analyser, whilst ions produced by background reactions can be monitored via the presence of contaminant peaks in the ToF-MS data. To reduce the probability of trapped ions undergoing reactive collisions with background contaminant species, the heat exchange device is operated during the reactions. Prior to the recording of experimental measurements, N_2 gas (cooled by liquid N_2) is constantly flowed through the device for at least two hours, reducing the amount of contaminants present to baseline levels. This process is also accompanied

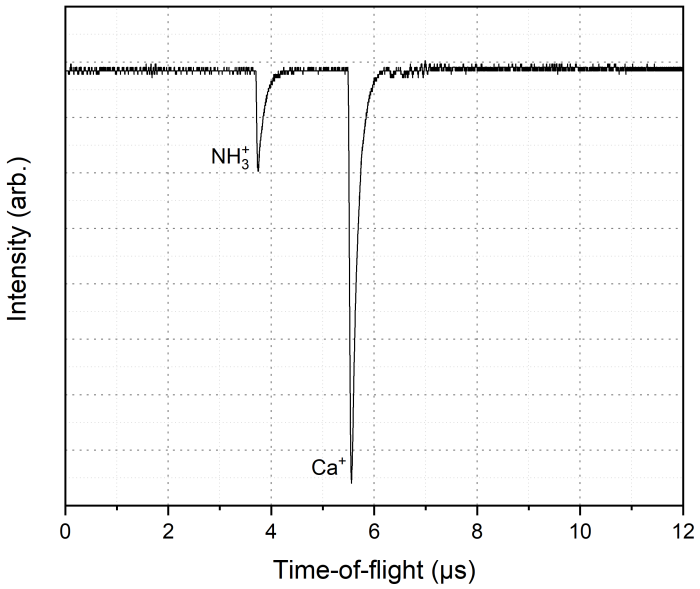


Figure 3.2: ToF trace recorded after the completion of a charge transfer reaction between Xe^+ ions and NH_3 neutrals. The absence of any other peaks—and, in particular, the absence of a peak at approximately 10 μs—confirms that all Xe^+ ions have reacted.

by a decrease in the pressure of the reaction chamber.

Background reaction studies of mono-component Ca^+ crystals show that, under the relevant experimental conditions, Ca^+ ions remain trapped with negligible ion loss for tens of minutes. As the timescale of the charge transfer reactions spans from tens of seconds to a couple of minutes—and the uncertainty with which the Ca^+ ions are established is ± 10 ions (see section 3.3)—the laser-cooled species are considered inert.

The sympathetically cooled species react with contaminant gases at a faster rate than Ca^+ ions. Xe^+ reacts with contaminant O_2 or pump-oil, but these reactions

are either absent or negligible over the course of several minutes, as determined from ToF-MS data. Kr^+ and Ar^+ ions react with trace amounts of background H_2O in the chamber, but this again occurs on a timescale slower than the charge transfer reactions. Assessed by ToF-MS information, any background reactions (when present) are explicitly accounted for in the analysis. In some cases, a small number of rare gas ions are found to react with residual ammonia neutrals in the chamber. This is demonstrated by the formation of a dark core prior to the admission of the ammonia reactants in the ion trap, as illustrated in the $t = 0$ crystal of Figure 3.1. When this occurs, the reaction between the rare gas ion and residual background ammonia molecules is quantified by MD simulations and accounted for in the resulting analysis (see equation 3.5).

3.2.2 Competitive reaction pathways

For the $Xe^+ + NH_3$ reaction system, only the charge transfer channel is exothermic ($\Delta H = -2.1\,\text{eV}$). All other reaction pathways (including hydrogen abstraction, $Xe^+ + NH_3 \rightarrow XeH^+ + NH_2$) have endoergicities $> 1\,\text{eV}$ [109]. The ToF-MS data recorded after completion of the reaction confirm that only Ca^+ and ammonia ions are present in the crystal, thus, excluding the formation of XeH^+ (or XeD^+) from hydrogen (deuterium) abstraction. As such, it is established that no competing reactions are occurring under the relevant experimental conditions.

The hydrogen abstraction channel is, however, exothermic for the $Kr^+ + NH_3$ reaction system, leading to products $KrH^+ + NH_2$. Previous studies at 300 K found electron transfer to be the dominant reaction pathway, with the competitive hydrogen abstraction channel identified as having a branching ratio of less than 1%—

equivalent to the reported uncertainty of the study [110]. Under the relevant experimental conditions of this work, at a temperature around 240 K, no KrH^+ or KrD^+ ions are detected in the ToF-MS data; the hydrogen abstraction channel is either entirely absent, or it plays such a negligible role that it falls within the experimental uncertainty. As such, it is assumed that every Kr^+ that reacts produces a charge transfer product ion ($NH_3{}^+$ or $ND_3{}^+$).

A more nuanced consideration of competitive reaction channels is required for the $Ar^+ + NH_3$ system. Previous experimental studies have identified three pathways following reactive $Ar^+ + NH_3$ collisions at 300 K [110],

$$Ar^+(^2P_{3/2}) + NH_3(^1A_1) \longrightarrow Ar + NH_3{}^+(^2A_2'') \quad (1)$$

$$Ar + NH_3{}^+(^2E) \longrightarrow Ar + H + NH_2{}^+ \quad (2)$$

$$ArH^+ + NH_2 \quad (3)$$

with reported branching ratios of 0.87, 0.07 and 0.06 (respectively). Reaction 1, the electron transfer process, has an exothermicity of $\Delta H = -5.60$ eV [111]. There is a discrepancy in the literature relating to the energy of the first electronically excited state of $NH_3{}^+$. The experimental work of Derai *et al.* place this channel approximately 4.7 eV above the energy of ground-state $NH_3{}^+$, making it accessible at 300 K [110]. The observed $NH_2{}^+$ products reported in a previous 300 K study are attributed to reaction 2: the dissociation of electronically excited $NH_3{}^+$ ions [110]. Theoretical calculations from two independent sets of studies report the adiabatic excitation energy to be approximately 6 eV [112, 113], suggesting that the electronically excited state of $NH_3{}^+$ is inaccessible at 300 K. Attempting to explain this discrepancy is beyond the scope of this thesis, however it is noted that no $NH_2{}^+$ products are observed in the ToF-MS measurements in this work. The formation of

excited state NH_3^+ (reaction 2) is either energetically closed under the experimental conditions of this work (at 204 K)—as predicted by the theory work—or is such a minor channel that it falls under the detection sensitivity level. The ToF-MS data also show no evidence of ArH^+ ions within the measurement resolution. While this channel is energetically open [113], the lack of any ArH^+ ions in the ToF-MS traces indicates that the branching ratio of the hydrogen abstraction channel (reaction 3) is < 0.05.

Even if a small number of ArH^+ product ions are formed, these do not affect the calculation of bimolecular rate coefficients for the charge transfer reaction. Only product ions that are formed in the dark core—i.e., species that have a mass-to-charge ratio below 40 u, which excludes any possible ArH^+products—are included in the analysis. No evidence of deuterium abstraction products, ArD^+, is detected within the experimental uncertainty, indicating that this is again a minor channel with a branching ratio of < 0.05.

3.2.3 Trapping efficiency

The trapping efficiency of the ammonia ions after their formation must also be considered. The trap depth for a given ion trapped in a linear Paul trap is calculated from the equation [114]

$$\phi(r_0) = \frac{Q^2 V_{\mathrm{RF}}^2}{4m\Omega_{\mathrm{RF}}^2 r_0^2} - \frac{\eta Q U_{\mathrm{end}} r_0^2}{2z_0^2}. \tag{3.1}$$

The first and second terms of equation 3.1 represent the radial plane (x-y) and axial (z) depths of the trap, respectively. Table 3.1 summarises the trap depths experienced by each ionic species involved in the ammonia charge transfer reactions. The respective exothermicities for the Xe^+, Kr^+ and Ar^+ reaction systems

are $\Delta H = -2.1\,\text{eV}$, $-3.84\,\text{eV}$ and $-5.60\,\text{eV}$ [109, 111], well within the trap depths experienced by the NH_3^+ and ND_3^+ product ions. Moreover, sympathetic cooling (elastic collisions with laser-cooled species) acts on the ammonia ions immediately after their formation to dissipate any kinetic energy. It is therefore assumed that all product ions are confined by the trapping potential.

Table 3.1: Trap depths experienced by the species involved in the charge transfer reactions.

Ion	Ca^+	Xe^+	Kr^+	Ar^+	NH_3^+	ND_3^+
Trap depth (eV)	2.9	0.46	1.0	2.9	7.5	6.3

Given the above discussion, the charge transfer reactions are considered to be one-to-one processes; every rare gas ion that reacts produces a charge transfer product ion (NH_3^+ or ND_3^+) that is efficiently confined in the linear Paul trap.

3.3 MD simulations

MD simulations are commonly used to model the properties of Coulomb crystals, such as ion numbers and temperatures [115]. The rate coefficients measured for the charge transfer reactions are extracted based on the comparison between the experimental Coulomb crystal images and the output of MD simulations. The software used is a custom-written MD simulation package that has been described in detail elsewhere [116]. Briefly, the input parameters of the code account for the experimental conditions experienced by Coulomb crystals in a linear Paul trap. The net force experienced by each ion is a sum of the trapping force (accounting for the interaction of the ion with the trap fields), the Coulomb force, a force term related to

the cooling mechanism, and a force term that models heating due to photon-recoil or collisions with background gas in the trap. The code integrates Newton's equations of motion to establish the positions and velocities of all ions in the crystal. The simulations yield a series of images that can be directly compared with experimental images (see Figure 3.3). Through quantitative comparison, complemented by ToF-MS data confirming the identities of the ions, the number of ions of each species within a Coulomb crystal at a given moment in time can be established.

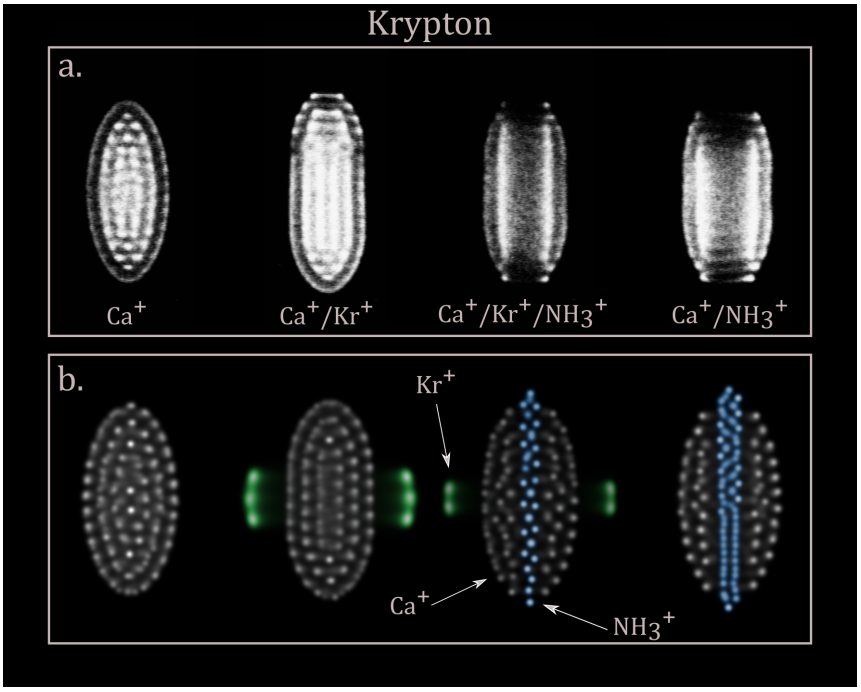


Figure 3.3: (a) Experimental images of a Ca^+ Coulomb crystal, a bi-component Ca^+ and Kr^+ crystal, a tri-component crystal midway through a charge transfer reaction, and a crystal at the completion of the reaction (i.e., when no Kr^+ reactants remain). (b) False colour MD simulations corresponding to the experimental Coulomb crystal images depicted in the top panel. The positions of the non-fluorescing co-trapped ions are explicitly shown in the simulations alongside the fluorescing Ca^+ ions. While these non-laser-cooled species are not visible in the experimental images, the positions and numbers of co-trapped species can be established from the MD simulations.

The accuracy of the comparison method for each ionic species taking part in the reactions, under the relevant experimental crystal sizes (typically a few hundred Ca^+ ions and up to a few hundred sympathetically cooled species) is ±10 ions for Ca^+, approximately ±50 ions for Xe^+, ±20 ions for Kr^+, ±30 ions for Ar^+ and ±5 ions for NH_3^+ and ND_3^+. The reduced accuracy in ascertaining the numbers of Xe^+ and Ar^+ ions arises from their mass-to-charge ratios. Xe^+ has a mass-to-charge ratio approximately three times larger than Ca^+, and as such the sympathetic cooling forces on the former are less efficient. As illustrated in Figure 3.4b, the Xe^+ ions do not adopt a crystallised structure, they instead form a sort of cloud around the crystallised Ca^+ ions. While Xe^+ ions are able to be confined by the trapping fields, their location in the crystal is such that they affect the positions of the laser-cooled Ca^+ ions to only a minor extent. A large number of Xe^+ ions need to be co-trapped in order for a noticeable change in the lattice positions of fluorescing Ca^+ ions to be observed. Conversely, with Ar^+ and Ca^+ exhibiting very similar mass-to-charge ratios (both species are singly charged with a mass of 40 u), they experience similar trapping forces and so are expected to be located at approximately the same distance from the trap axis. As the cooling lasers are applied from one direction, radiation pressure induces a spatial separation between the equilibrium positions of Ca^+ and Ar^+ ions in the crystal. In the orientation depicted in Figure 3.4c and d, Ar^+ ions are preferentially located at the top of the crystal. The mass-to-charge ratio of NH_3^+ (or ND_3^+) is approximately half that of Ca^+, resulting in the confinement of ammonia ions on the trap axis and giving rise to what is termed a "dark core" in the crystal. Comparing the average width of the dark core between experiments and simulations allows the number of ammonia ions to be established within ±5 ions. Owing to this high sensitivity—and taking into consideration that the reactions are

one-to-one processes—reaction rate coefficients can be accurately calculated.

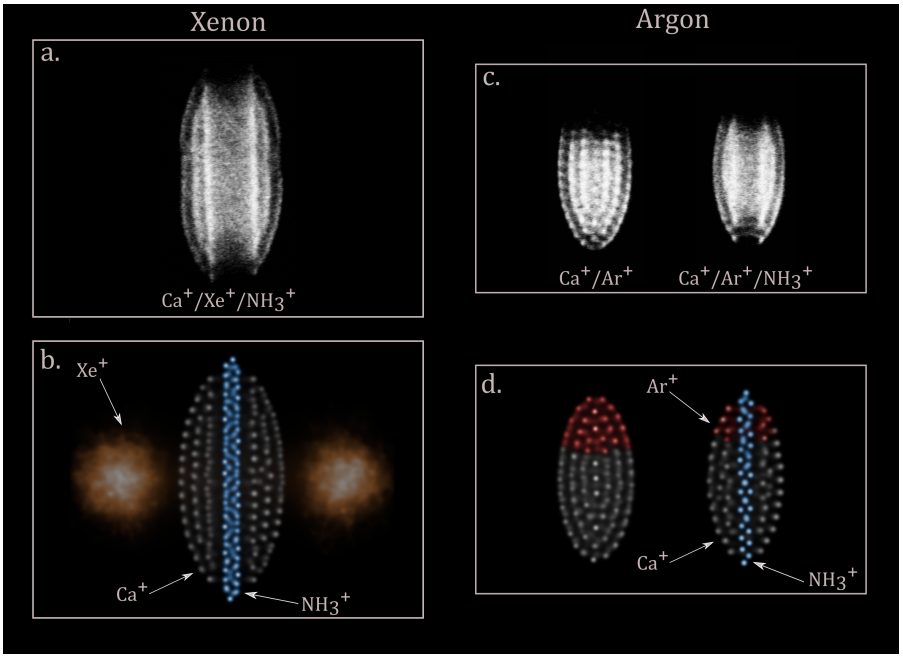


Figure 3.4: (a) Experimental image of a tri-component Ca^+, Xe^+ and $NH_3{}^+$ crystal midway through a charge transfer reaction. (b) False colour MD simulation corresponding to the experimental Coulomb crystal image depicted in the panel above. The non-crystallised cloud of Xe^+ ions is shown in orange. (c) Experimental images of a bi-component Ca^+ and Ar^+ crystal and a crystal midway through a reaction. (d) MD simulations corresponding to the experimental Coulomb crystals of panel (c). The confinement of Ar^+ on the top part of the image can be seen in both experimental and simulated images.

Note that one parameter that needs to be adjusted in the MD simulations to correctly replicate the experimental conditions is the geometric factor, η. As it compensates for the non-ideal geometry of the trap, it can slightly shift with time, and therefore needs frequent optimisation. A number of iterative comparisons between simulated and experimental crystals with different sizes, V_{RF} and U_{end} is needed to establish its value, which usually ranges from 0.26–0.28.

3.4 Reaction rate coefficients

The kinetic model employed to calculate experimental reaction rate coefficients is described below, for the $Xe^+ + NH_3$ reaction system. All charge transfer reactions follow the same model. As detailed in section 3.2, the reactions can be described as one-to-one processes. As such, they follow an equation of the form

$$\frac{\mathrm{d}[Xe^+]}{\mathrm{d}t} = -\frac{\mathrm{d}[{NH_3}^+]}{\mathrm{d}t} = -k[Xe^+][NH_3], \tag{3.2}$$

where $[Xe^+]$ and $[NH_3]$ represent the number densities of each reactant species and k is the bimolecular reaction rate coefficient. Ammonia is introduced effusively into the chamber via a high-precision leak valve. Assuming a constant flow of ammonia during the reactions, equation 3.2 can be rearranged into a pseudo-first order equation

$$[{NH_3}^+]_t = [Xe^+]_0 \left(1 - e^{-k't}\right), \tag{3.3}$$

where k' is the pseudo-first order rate coefficient given by

$$k' = k[NH_3]. \tag{3.4}$$

k' is calculated by plotting the number of ${NH_3}^+$ ions established from the comparison with MD simulations as a function of time (see Figure 3.5). The data points are fit to an exponential growth curve that follows the equation

$$[{NH_3}^+]_t = [Xe^+]_0(1 - e^{-k'(t-t_0)}) + [{NH_3}^+]_0. \tag{3.5}$$

The term $[{NH_3}^+]_0$ is included in equation 3.5 to account for any ammonia ions present in the dark core prior to admitting the reactants to the ion trap volume (see, for example, Figure 3.1 at $t = 0$). This explicitly allows for the possibility of

trace amounts of ammonia contaminants being present in the chamber. The first few data points recorded for each reaction do not fit well to the exponential growth model of equation 3.3. This is due to the finite time required for the ammonia partial pressure to reach the desired value. The t_0 term in equation 3.5 accounts for the uncertainty in the time that the charge transfer reaction started; it allows for a delay between when the leak valve is opened and when the partial pressure of ammonia reaches the desired stable value in the chamber. To establish when uniform conditions have been achieved, equation 3.5 is converted to a logarithmic form and, subsequently, the data are fit to the linear equation

$$ln(1 - \frac{[NH_3{}^+]_t - [NH_3{}^+]_0}{[Xe^+]_0}) = -k'(t - t_0). \tag{3.6}$$

Points that clearly deviate from the linear fit of equation 3.6 at early reaction times are discarded. As illustrated in Figure 3.5a, the logarithmic form facilitates the easier identification of these points. However, the linear fit is used only to establish when the partial pressure of ammonia became stable, with the exponential form of the graph (Figure 3.5b) used for the calculation of the pseudo-first order rate coefficients.

Bimolecular rate coefficients, k, are calculated from the pseudo-first order rate coefficients, k', using the equation

$$k = \frac{k'}{[NH_3]} = \frac{k'}{N/V} = \frac{k' k_B T}{P}, \tag{3.7}$$

where T is the temperature of the thermal ammonia molecules (290–293 K in the laboratory) and P is the partial pressure of ammonia in the ion trap chamber. A bimolecular rate coefficient is calculated for each reaction measurement. The final k value reported represents the average of all rate coefficients calculated for a

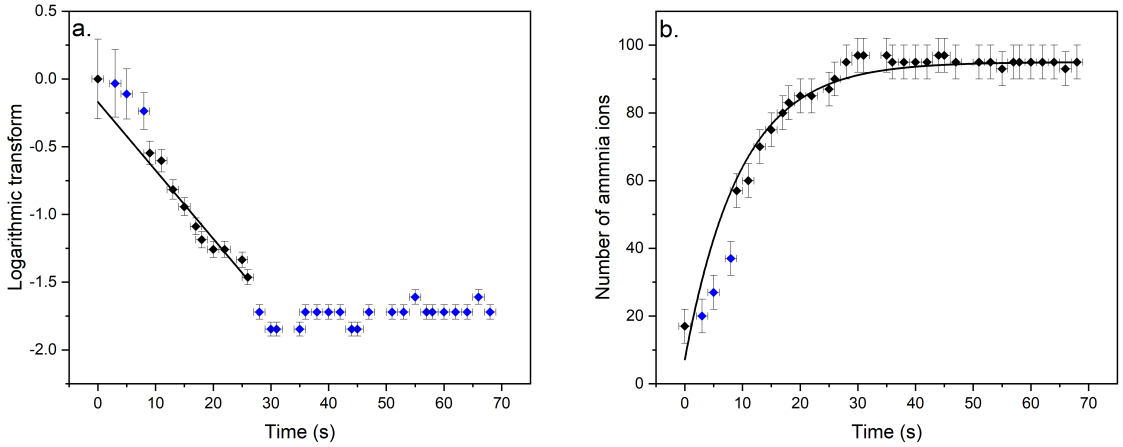


Figure 3.5: (a) Logarithmic form of equation 3.6. The first three points (after the assigned time zero of the reaction) are discarded as they evidently deviate from the linear fit. The later points (appearing as a horizontal line) deviate from the earlier linear trend, as the reaction has gone to completion and so the number of ammonia ions is no longer changing. (b) Exponential growth fit to equation 3.5, taking into account the data points recorded once conditions were stable. Error bars of E_y = ±5 ions and E_x = ±1 s account for the accuracy of the MD simulations and experimental uncertainty in the reaction time, respectively.

given system (i.e., considering the values established for every repeat measurement undertaken). For the $Xe^+ + NH_3/ND_3$ reactions, uncertainties are calculated using the propagation of errors of the respective uncertainties of the pseudo-first order equation fit on the data points, $\sigma_{k'}$, and the experimental reading of the partial pressure, σ_P

$$\sigma_k = k\sqrt{(\frac{\sigma_{k'}}{k'})^2 + (\frac{\sigma_P}{P})^2}. \tag{3.8}$$

For the Kr^+ and Ar^+ reaction systems, there is a higher statistical error associated with the measured k values. As such, uncertainties are stated as the statistical error (one standard deviation).

To confirm the validity of this approach, bimolecular rate coefficients are also cal-

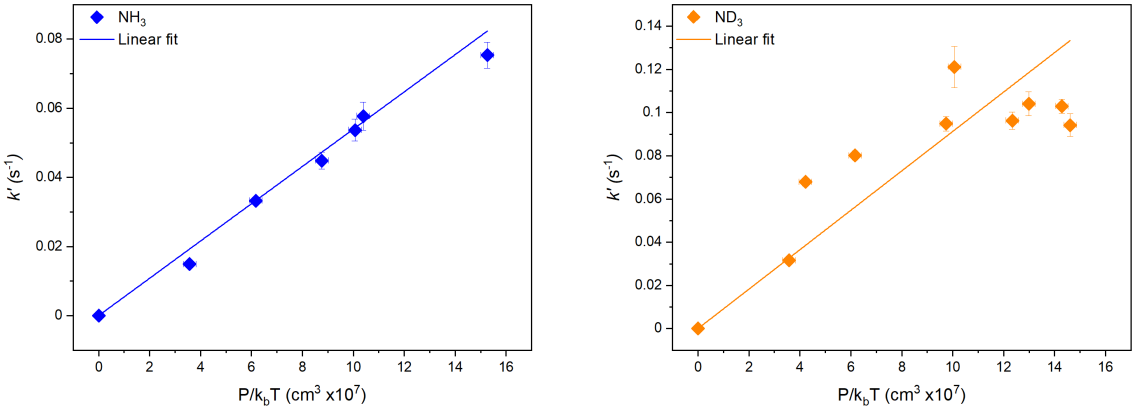


Figure 3.6: Pseudo-first order rate coefficients calculated for the Kr^+ reactions are plotted as a function of the ammonia reactant partial pressure. The gradient of the linear fit corresponds to the bimolecular rate coefficient, k_{lin}.

culated by plotting the pseudo-first order rate coefficients (k') as a function of the partial pressure of ammonia. Figure 3.6 illustrates the linear correlation between partial pressure and k', with the gradient of the line corresponding to the bimolecular rate coefficient. While there is excellent agreement between the k values obtained from the two approaches (see Table 3.2), there is a higher uncertainty associated with the rate coefficients obtained from the averaging method. Due to the limited ability to vary the partial pressure of the ammonia reactants (it can only be adjusted between 1×10^{-9} and 5×10^{-9} mbar), the linear fit method is simply used as a complementary way of examining the data. The rate coefficients obtained from both methods provide confirmation that the findings are robust. However, only rate coefficients calculated from the averaging method are used for discussion in later chapters.

Table 3.2: Pseudo-first order (in s^{-1} $\times 10^{-2}$), k', and bimolecular rate coefficients (in $cm^3\,s^{-1}$ $\times 10^{-9}$) calculated for the reaction systems of interest using the average, k, and linear correlation, k_{lin}, methods. The experimental uncertainty in the last decimal place is stated in parentheses; for example, $k = (0.36 \pm 0.02) \times 10^{-9}$ $cm^3\,s^{-1}$ for the $Xe^+ + NH_3$ system at 260 K. The number of points and weighted temperatures of each reaction system are also included.

Reaction system	k'	k	k_{lin}	No. of Points	T (K)
$Xe^+ + NH_3$	3.3(2)	0.36(2)	0.37(1)	4	260
$Xe^+ + ND_3$	11(2)	1.2(2)	0.9(2)	4	255
$Kr^+ + NH_3$	4.7(2)	0.51(5)	0.54(2)	6	246
$Kr^+ + ND_3$	8.8(4)	1.0(3)	0.9(1)	9	239
$Ar^+ + NH_3$	9.0(8)	1.4(2)	1.3(1)	4	204
$Ar^+ + ND_3$	12(1)	1.7(5)	1.5(2)	6	194

3.4.1 Reaction temperature

To compare the calculated reaction rate coefficients with capture theory models, a collision temperature needs to be assigned to the systems. The temperature of the ions (laser- or sympathetically cooled) can be established using the output velocities from the MD simulations. As Coulomb crystals are systems not in true equilibrium, the term "temperature" is used as an equivalent of the kinetic energy of the trapped ions. Considering the dependence of the micromotion on the position of the ions, as discussed in section 2.1, a range of velocities, and therefore temperatures, is expected throughout a Coulomb crystal. An effective temperature is assigned to a crystal by converting the average kinetic energy of the ions to units of Kelvin, using $T = \overline{E}_{kin}/k_B$.

Accounting for both the secular motion and micromotion of the sympathetically

cooled reactant ions, their effective temperature is estimated to be around 24 K, 13 K and 3 K for Xe^+, Kr^+ and Ar^+, respectively. The ammonia neutrals have thermal energies, ranging between 290–293 K. A weighted average between the ammonia temperature, T_a, and the effective temperature of the sympathetically cooled, rare gas ions, T_{Rg}, represents the collision temperature for each reaction system. It is given by

$$T_{\text{weighted}} = \frac{m_a T_{Rg} + m_{Rg} T_a}{m_{Rg} + m_a}. \tag{3.9}$$

The assigned temperature values are summarised in Table 3.2.

Chapter 4

Capture theories and inverse KIEs

The experimentally measured rate coefficients presented in Chapter 3 are discussed within the framework of capture theory models, often used to describe the behaviour of ion-molecule reactions. The six ammonia reaction rate coefficients are suppressed in comparison with classical and quantum capture models. In addition, for all systems, an inverse KIE is observed, the magnitude of which depends on the mass of the rare gas reactant. Complemented by detailed *ab initio* calculations and a one-dimensional quantum-mechanical (QM) model, a tentative explanation for these observations is given. The findings are further discussed in the context of astrochemical models that often adopt capture theories to predict low-temperature reaction rate coefficients of experimentally unmeasured reactions.

4.1 Capture theories

Two capture theory models are employed, namely the ADO and the ACCSA model. ADO is a classical capture theory that describes the interactions between polar molecules and ions, taking into account properties of the neutral polar reactant (such as dipole moment) and assuming a classical distribution of rotational state

populations [5]. ADO rate coefficients are calculated in SI units using the equation

$$k_{\mathrm{ADO}} = q\sqrt{\frac{\pi\alpha}{\varepsilon_0\mu}} + \frac{qc\mu_D}{\varepsilon_0}\sqrt{\frac{1}{2\pi\mu k_B T}}, \tag{4.1}$$

where q is the charge of the ion, α the polarisability of the neutral molecule, ε_0 the permittivity of free space, μ the reduced mass of the ion-neutral system, μ_{D} the dipole moment of the neutral species and T the temperature of the reaction. The parameter c accounts for the average orientation of the dipole of the neutral species during the reaction and depends on the temperature of the system and the ratio $\frac{\mu_{\mathrm{D}}}{\alpha^{1/2}}$ [117]. The first term of equation 4.1 is the Langevin reaction rate coefficient. The ADO model extends Langevin's theory, developed for reactions between ions and non-polar molecules, by adding a term to account for temperature and dipole moment considerations. The form of equation 4.1 results in an inverse temperature dependence, as expected for reactions between ions and polar molecules. As it assumes a classical distribution of rotational states, ADO theory is better suited for describing systems at energies near 300 K, rather than low-temperature systems where only few rotational states are occupied. Quantum capture theories, such as the ACCSA model, overcome this limitation by accounting for the contribution of each individual rotational state to the overall reaction rate coefficient.

ACCSA is a rotationally adiabatic quantum capture theory, developed for symmetric top molecules such as NH_3 or ND_3 [118]. The model takes into account the quantum numbers (J, j, K, Ω), where J is the total angular momentum, j the molecular angular momentum, K the projection of j onto the molecular-fixed axis, and Ω the projection of J and j onto the body-fixed axis. A reaction rate coefficient is calculated for each rotational state and their average contribution yields the overall rate coefficient. The ACCSA model predicts that lower rotational states have higher

rate coefficients, resulting again in the inverse temperature behaviour of ion-polar molecule reactions. A brief description of the calculation is given in Appendix A (more details can be found elsewhere [119]).

While the ACCSA model provides a more complete description of the reaction, ADO is expected to give a good approximation of rate coefficients at temperatures close to 300 K. As the charge transfer reactions are conducted at collision energies below 300 K, but under conditions that are still considered "warm" (at temperatures ranging from 194–260 K), both ADO and ACCSA models are employed. Table 4.1 summarises the parameters used to calculate the capture theory rate coefficients.

Table 4.1: Polarisabilities [120, 121], dipole moments [122, 121] and c parameters used to calculate the ADO rate coefficients. The parameter c varies with the weighted temperature of each reaction system [117]. The rotational constants A and B [123] are parameters included in the ACCSA rate coefficient calculations.

Isotopologue	α (cm^3)	μ_D (D)	c	A (cm^{-1})	B (cm^{-1})
NH_3	2.16×10^{-24}	1.47	0.227–0.234	6.19600	9.44430
ND_3	1.88×10^{-24}	1.50	0.232–0.239	3.14420	5.14280

4.2 Experimental results

Table 4.2 summarises the experimentally derived rate coefficients for the six charge transfer reactions studied as well as the predictions from the ADO and ACCSA capture theory models. The $Xe^+ + NH_3$, $Kr^+ + NH_3$ and $Ar^+ + NH_3$ reactions have been studied previously at 300 K, in ICR [110] and SIFT [124] experiments. The rate coefficients reported in these studies are also included in Table 4.2.

Table 4.2: Experimental, ADO, ACCSA and QM rate coefficients (in $cm^3\,s^{-1} \times 10^{-9}$) for the charge transfer reactions between Xe^+, Kr^+ or Ar^+ ions and the two ammonia isotopologues of interest. Previous work conducted at 300 K is included for comparison.

Reaction system	k_{exp}	k_H/k_D	k_{ADO}	k_{ACCSA}	k_{QM}	T (K)
$Xe^+ + NH_3$	0.6(1)[a]		1.65	2.13		300
	0.8(2)[b]					
	0.36(2)		1.74	2.25	0.28	260
$Xe^+ + ND_3$	1.2(2)	0.30(5)	1.60	2.12	0.25	255
$Kr^+ + NH_3$	0.8(2)[a]		1.71	2.20		300
	0.7(1)[b]					
	0.51(5)		1.82	2.38	0.34	246
$Kr^+ + ND_3$	1.0(3)	0.5(2)	1.69	2.26	0.30	239
$Ar^+ + NH_3$	1.8(4)[a]		1.86	2.40		300
	1.4(2)		2.11	2.78	0.38	204
$Ar^+ + ND_3$	1.7(5)	0.8(3)	2.00	2.70	0.35	194

[a]Derai *et al.* [110], [b]Giles *et al.* [124]

Figures 4.1, 4.2 and 4.3 plot the experimentally derived rate coefficients for the Xe^+, Kr^+ and Ar^+ reaction systems, respectively, as a function of temperature. The calculated ADO and ACCSA predictions are also plotted, alongside rate coefficients obtained from a one-dimensional QM model (see section 4.3). In every instance, the predictions from capture theory models are higher than the experimentally measured

rate coefficients. Of the six reactions considered, only those involving argon ions ($Ar^+ + ND_3$ at 194 K in this work, and $Ar^+ + NH_3$ at 300 K recorded utilising the ICR technique) yield rate coefficients that are within the uncertainty range of the ADO predictions. Even then, the more robust ACCSA model predicts a higher rate coefficient.

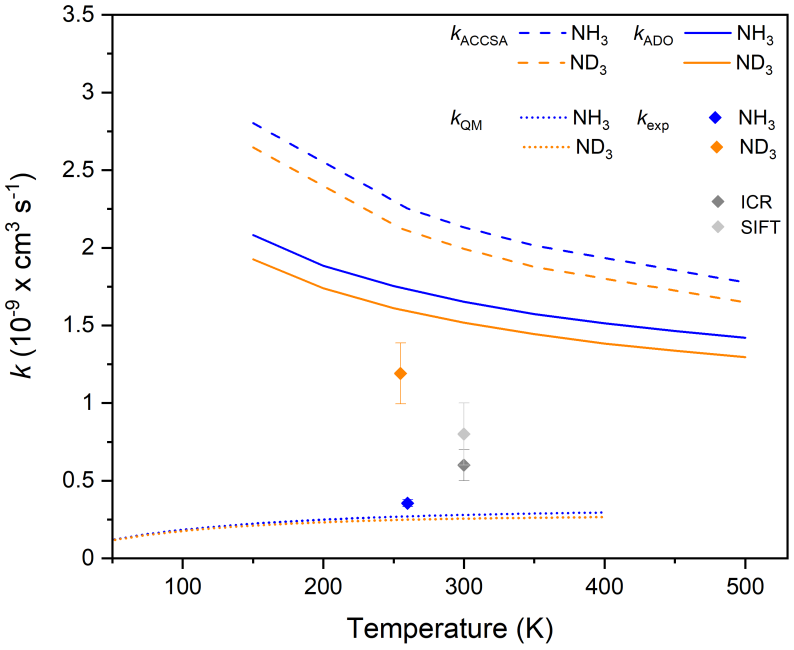


Figure 4.1: Charge transfer rate coefficients for the $Xe^+ + NH_3$ (blue) and $Xe^+ + ND_3$ (orange) reaction systems, as established from capture theory models (ACCSA and ADO), from a QM model, and from experimental measurements. Previous work conducted at 300 K is included for comparison (grey) [110, 124]. Error bars indicate the uncertainty in the experimental rate coefficients (see section 3.4 and previous work [110, 124]).

The experimental rate coefficients reported in this work, recorded at temperatures between 194 K and 260 K, are consistently lower than the rate coefficients reported

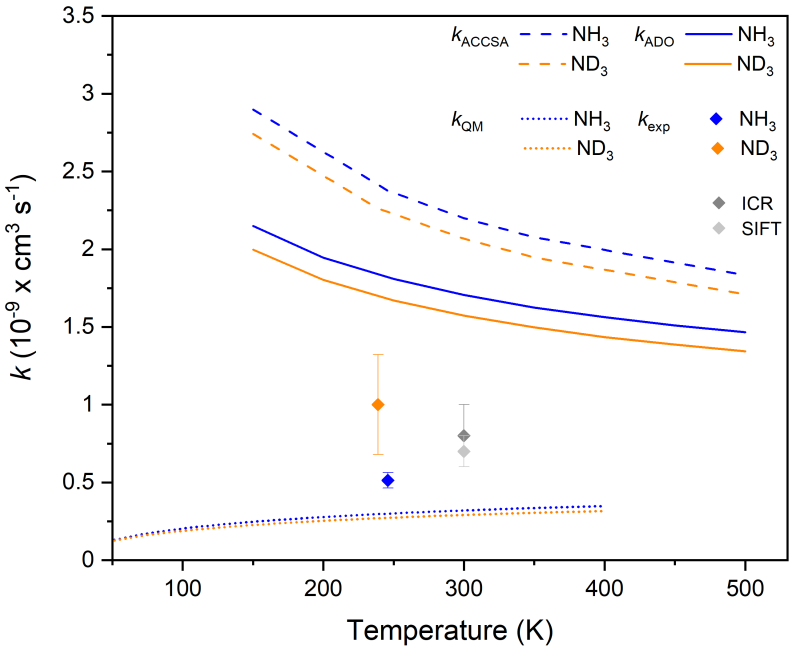


Figure 4.2: Charge transfer rate coefficients for the $Kr^+ + NH_3$ (blue) and $Kr^+ + ND_3$ (orange) reaction systems, as established from capture theory models (ACCSA and ADO), from a QM model, and from experimental measurements. Previous work conducted at 300 K is included for comparison (grey) [110, 124].

from the ICR and SIFT experiments at 300 K. It is, however, difficult to directly compare measurements recorded using ICR or SIFT with those recorded using Coulomb crystals, owing to the different experimental conditions involved. For example, while here the ammonia reactants are thermal, the ionic reactants are effectively stationary (i.e., the two reactants are not in thermal equilibrium). The charge transfer reactions are also carried out under ultra-high vacuum conditions (on the order of 1×10^{-9} mbar), in what has been described as a nearly perturbation-free environment [39, 40]. In comparison, for example, SIFT measurements are typically

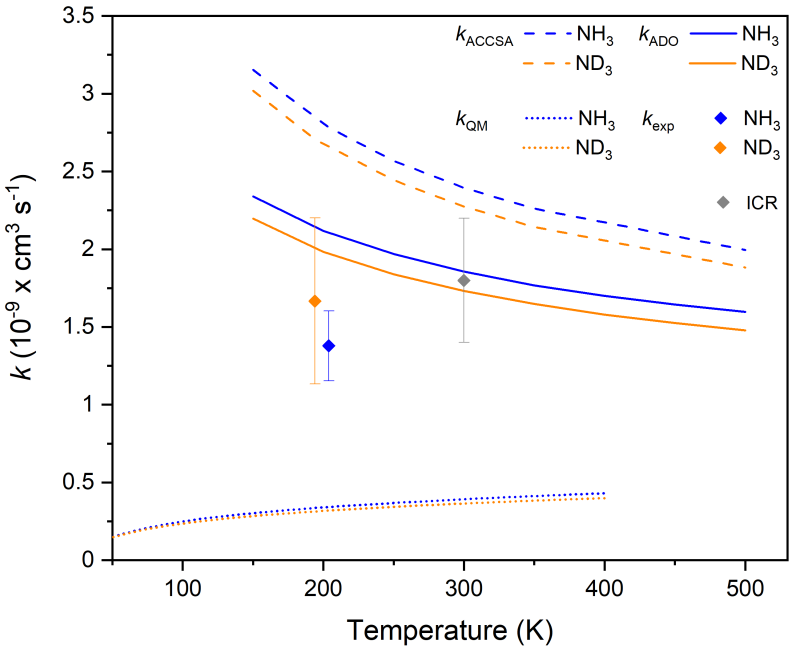


Figure 4.3: Charge transfer rate coefficients for the $Ar^+ + NH_3$ (blue) and $Ar^+ + ND_3$ (orange) reaction systems, as established from capture theory models (ACCSA and ADO), from a QM model, and from experimental measurements. Previous work conducted at 300 K is included for comparison (grey) [110].

carried out in a helium buffer gas, at pressures that are many orders of magnitude higher (approximately 0.7 mbar) [124]. It is therefore difficult to directly compare findings reported from these different experimental methods.

Figures 4.1, 4.2 and 4.3 also illustrate that the three rare gas ions react faster with ND_3 than NH_3, resulting in the observed KIEs. KIEs are reported as the ratio between the rate coefficients of the hydrogenated and deuterated reaction systems, k_H/k_D. Generally, they emerge from differences in the zero-point energy between isotopologues (a D-substituted molecule, due to its heavier reduced mass, will have

lower zero-point energy) as well as differences in the likelihood that reactants can tunnel through any reaction barriers [125]. The probability of tunneling always favors the lighter hydrogen-containing species, enhancing k_H. In most cases, D-substitution leads to a decrease in the rate of a reaction, with $k_H/k_D > 1$, known as a "normal" KIE. When $k_H/k_D < 1$, the KIE is referred to as "inverse".

Primary KIEs are observed when the D-substitution is made in a bond that breaks during the reaction. Generally, they are normal KIEs (i.e., $k_H/k_D > 1$) and their magnitude ranges widely ($k_H/k_D = 1.0 - 16$) [126]. Secondary KIEs arise when the isotopic substitution is made in a bond that does not break during the rate-determining step of a reaction. Secondary KIEs are much less pronounced than primary effects, typically ranging between $k_H/k_D = 1.1-1.2$ for normal and $k_H/k_D = 0.8-0.9$ for inverse effects [125]. As no N–H or N–D bonds are broken in the course of the charge transfer reaction, the KIE is classified as secondary.

There is a clear periodic trend in the magnitude of the inverse KIE observed in the charge transfer reactions. The heaviest (Xe^+) ion shows the strongest effect, with $k_H/k_D = 0.30(5)$, a very pronounced inverse secondary KIE. On the contrary, the lightest (Ar^+) ion displays a much weaker effect, with $k_H/k_D = 0.8(3)$, with a normal KIE within the stated uncertainty range. The inverse KIE observed for Kr^+ falls in between the Xe^+ and Ar^+ cases, with $k_H/k_D = 0.5(2)$, still a substantial effect. This trend can be clearly identified in Figure 4.4, where the inverse KIE is plotted as a function of the ionic mass.

Both ADO and ACCSA models predict a weak normal KIE ($k_H/k_D \approx 1.1$), the magnitude of which does not vary significantly with the mass of the rare gas ion. The small difference in the predicted rate coefficients arise from differences in the

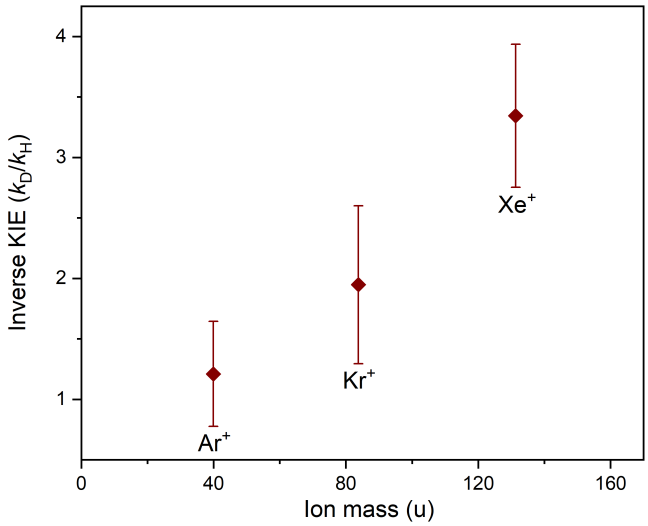


Figure 4.4: Inverse KIEs observed for the charge transfer reactions between Xe^+, Kr^+ or Ar^+ ions and the two ammonia isotopologues (NH_3 or ND_3). The magnitude of the effect is plotted as a function of the mass of the rare gas ion, showing the mass-dependent trend. The error bars arise from the uncertainty in the experimental rate coefficients. Note that each reaction system was studied at a different temperature (see Table 4.2).

polarisability and dipole moment of the isotopologues in addition to their different masses (see Table 4.1). Neither the presence of an inverse KIE nor the magnitude of the rate coefficients can be explained within the framework of capture theories; the charge transfer reactions are evidently not capture-limited.

4.3 Theoretical work

To obtain a more detailed picture of the experimentally studied charge transfer reactions, collaborative theory work was conducted. PESs were built from high-level

ab initio calculations performed on the $Rg^+ + NH_3$ systems and a one-dimensional QM model was employed to generate reaction rate coefficients. A brief summary of the PES calculations and the QM model is given in this section. Although not part of the work undertaken in this thesis, the theory is included here to facilitate the discussion of the experimental results in the following sections. All theory work described in this subsection was carried out by a collaborator, Prof. Jérôme Loreau, at KU Leuven. Further details can be found elsewhere [127, 113].

4.3.1 *Ab initio* calculations

PESs were constructed by means of the multi-configurational self-consistent field method (MCSCF) and the multi-reference configuration interaction (MRCI) method including the Davidson correction (MRCI+Q), as implemented in the MOLPRO quantum chemistry package [128, 129, 130]. The N–H bond length is similar for NH_3 and NH_3^+, and as such this distance is kept fixed (at $1.92\,a_0$). The PESs therefore depend on four coordinates: R is the length of the vector $\mathbf{R}$ describing the position of the $Rg^{(+)}$ atom with respect to the centre of mass of $NH_3^{(+)}$, θ (with $0° \leq \theta' \leq 180°$) is the angle between the vector $\mathbf{R}$ and the C_3 symmetry axis of the ammonia, and φ (with $0° \leq \varphi' \leq 360°$) is the angle of rotation of this vector around the C_3 axis. Finally, the angle ρ describes the umbrella motion of ammonia. For NH_3, the equilibrium value is $\rho = 112.1°$; NH_3^+ is planar, with $\rho = 90°$. The charge transfer dissociation channels $Rg + NH_3^+$ and $Rg^+ + NH_3$ correspond to the ground and first excited states of the complex, respectively. There are no other molecular states that energetically lie between the two charge transfer channels.

The most favourable orientation for charge transfer is when the Rg^+ ion approaches

the N-atom end of the ammonia molecule along the dipole axis ($\theta = 180°$). Figure 4.5 compares the PESs of the charge transfer channels for the $[NH_3Rg]^+$ systems for this orientation and at the equilibrium umbrella angle $\rho = 112°$.

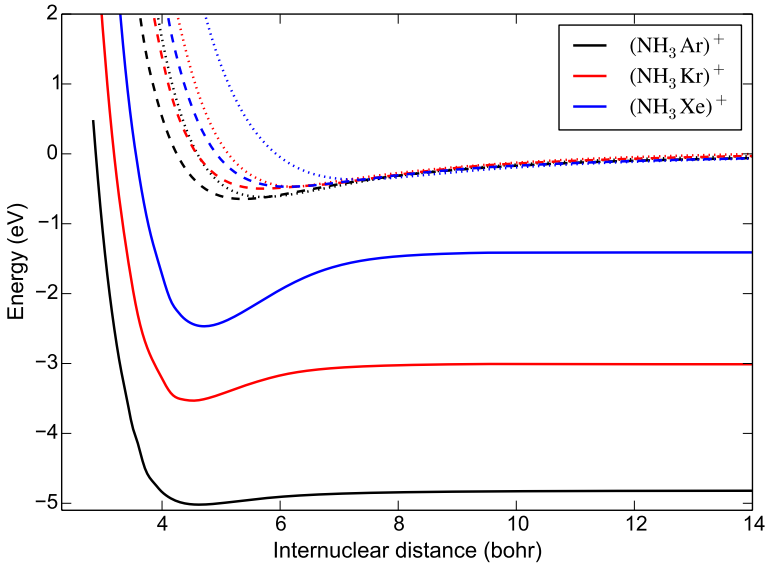


Figure 4.5: One-dimensional cuts of the PESs of the $[NH_3Rg]^+$ complexes relevant to the charge transfer process, as a function of the distance R between the Rg^+ ion and the centre of mass of NH_3. Solid lines correspond to the ground-state PESs dissociating into $NH_3^+ + Rg(^2S)$; dashed and dotted lines correspond to the excited state PESs dissociating into $NH_3 + Rg^+(^2P)$. (Although not present under the relevant experimental conditions, the upper spin-orbit state, $Rg^+(^2P_{1/2})$, was also included in the calculations.) The zero of energy is set at the entrance channel, $NH_3 + Rg^+(^2P)$. The angles are $\theta = 180°$ and $\phi = 0°$, corresponding to the Rg^+ ion approaching the N atom of NH_3 along the C_3 axis. The umbrella angle is fixed to the equilibrium value of NH_3, $\rho = 112°$ [113].

The non-adiabatic couplings were calculated and are represented in Figure 4.6. Their shape is similar for all three systems. It is broad and weak, corresponding to the fact that the PESs do not cross. However, the maximum of the coupling occurs at shorter distances for the lighter systems. The position of the maximum is at

$R = 4.5\,a_0$ for $[NH_3Ar]^+$ (close to the turning point in the entrance channel). Upon charge transfer, the umbrella angle is relaxed from $\rho = 112°$ (the equilibrium value of NH_3) to $\rho = 90°$ (the equilibrium value of $NH_3{}^+$). However, the calculations show that the non-adiabatic coupling depends only very weakly on the umbrella angle.

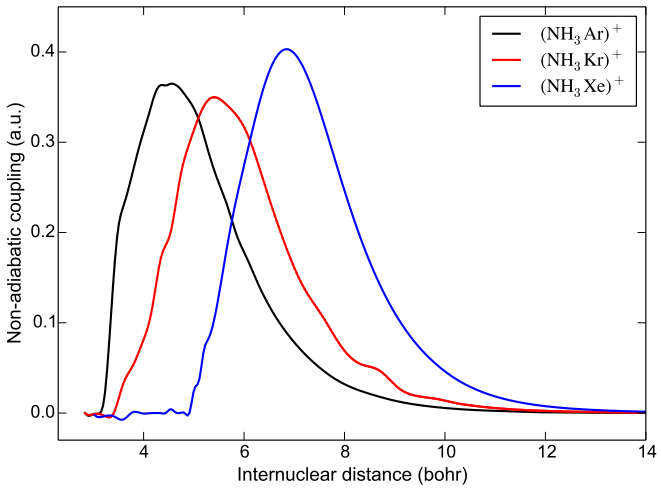


Figure 4.6: Non-adiabatic coupling between the pairs of potential energy curves shown in Figure 4.5, for three different charge transfer systems of interest [113].

4.3.2 QM model

The one-dimensional QM dynamical model corresponds to the most favourable approach along the C_3 axis of NH_3 represented in Figure 4.5. The radial time-independent Schrödinger equation was solved using the close-coupling formalism to obtain reaction cross sections on an energy grid, from which rate coefficients were calculated [131, 132]. The results are included in Table 4.2 and are plotted along with the experimental and capture theory rate coefficients in Figures 4.1, 4.2 and 4.3. As seen, the QM coefficients are much smaller than those obtained with capture

theory. As there is only a weak non-adiabatic coupling between the PESs, not all collisions lead to a reaction. The results are also below the experimental rate coefficients, and predict once again a normal KIE. A limitation of the one-dimensional QM model is that it does not take into account the increase in lifetime that occurs due to intramolecular vibrational redistribution (IVR) between different degrees of freedom of the reaction complex. In the QM model, if charge transfer does not take place within one vibrational period along the reaction co-ordinate, then no products are predicted. However, the effect of IVR is that the complex is much longer lived than one vibrational period, enhancing the probability that charge transfer occurs in the lifetime of the complex. This explains why the QM rate coefficients are lower than those observed experimentally.

4.4 Proposed explanation

Capture theories assume that any collision that leads to complex formation will yield products with unit probability. For reactions that proceed slower than capture theory predictions, a more nuanced approach needs to be adopted to describe the likelihood of product formation. For example, the presence of a submerged barrier along the reaction coordinate will increase the likelihood that a reaction complex dissociates back to reactants, thereby decreasing the rate coefficient for product formation [10].

The charge transfer reactions of the ammonia isotopologues and the rare gas ions are evidently not capture-limited. The presence of an inverse KIE as well as its dependence on the mass of the rare gas ion cannot be explained within the framework of capture theory models. *Ab initio* calculations confirm that the mechanism of

electron transfer is not straightforward as no energetically accessible crossing points are identified between the reactant and product PESs, for a wide variety of θ, φ and ρ. The one-dimensional QM model successfully predicts some of the experimental outcomes, but fails in others. The QM rate coefficients are systematically smaller than the ones obtained by capture theories (as well as the experimental measurements). In other words, not all collisions are reactive, which can be explained by the weak coupling between the PESs. The QM rate coefficients decrease with increasing mass of the rare gas ion, corresponding to the experimental observations (for charge transfer with NH_3). The QM model also suggests that the rate coefficients will decrease with decreasing temperature (for all systems), as opposed to the predictions of capture theories. However, the QM model predicts that the rate coefficient should be smaller for ND_3 than for NH_3, which shows that this model is insufficiently detailed to explain the observed inverse KIE.

There are several steps involved in the transfer of an electron from a neutral ammonia molecule to a rare gas ion, as set out in the general reaction scheme

$$Rg^+ + NH_3 \underset{k_{-1}}{\overset{k_1}{\rightleftharpoons}} [Rg\text{–}NH_3]^+ \xrightarrow{k_2} Rg + {NH_3}^+.$$

k_1 represents the rate of capture, k_{-1} represents the rate of dissociation of the complex back to reactants, and k_2 represents the rate of charge transfer within the complex and the subsequent formation of products. It is the relative magnitudes of k_1, k_{-1} and k_2, which are related to the properties of the $[Rg\text{–}NH_3]^+$ complex, that dictate whether the reaction complex proceeds to product formation, or whether it falls apart to re-form reactants.

For a process that obeys pure capture theory, $k_2 >> k_1 > k_{-1}$. Complex formation

(k_1) is the rate-limiting step; with k_2 being much larger than k_{-1}, every captured complex proceeds to products. In the systems examined here, the rate of charge transfer is not significantly larger than k_1 and k_{-1}. Hence the experimental rate coefficients for charge transfer are lower than capture theory predicts. The key factor then becomes the competition between k_2, product formation, and k_{-1}, dissociation of the complex back to reactants.

k_{-1} will predominantly depend on the vibrational motion of the ammonia entity. To first order, for a simple ion-atom collision (under low pressure conditions) k_{-1} can be approximated as having a magnitude comparable to one vibrational period along R, because there is nothing to stop the collision partners rebounding off the inner repulsive wall and re-dissociating. However, for polyatomic species, such as NH_3 or ND_3, the lifetime of the complex is longer because the kinetic energy initially directed along the collision co-ordinate can be dispersed into other low-energy vibrational modes of the complex. This so-called IVR process can have the effect of lowering k_{-1}.

The very different vibrational frequencies associated with the hydrogenated and deuterated ammonia moieties in the reaction complex are proposed to give rise to the observed isotope effect. It has been previously established that the rate of IVR in polyatomic molecules and complexes depends on the density of vibrational states within the complex [133, 134, 135]. It is also known that deuteration can lead to faster IVR, because the greater mass of deuterium reduces vibrational frequencies, increasing the density of vibrational states at a given energy [136, 137, 138, 139]. Not only is the rate at which the energy is dispersed by IVR likely to be greater for the deuterated complex, but also (because the energy is dispersed into a greater

number of vibrational states), the statistical rate at which the energy finds its way back into the dissociation co-ordinate is lower. As such, the lifetime of the deuterated complex is expected to be longer than that of the hydrogenated complex, lowering k_{-1}. This, in turn, sees a greater proportion of $[Rg–ND_3]^+$ complexes proceed to products, yielding a faster rate coefficient for charge transfer when compared to the $[Rg–NH_3]^+$ system. With a greater k_2, the difference between k_{-1} for ND_3 and NH_3 has a less important effect on the overall rate coefficient and therefore the inverse kinetic isotope effect is less marked. As such, a greater k_2 for Ar^+ when compared to Kr^+ and Xe^+ would explain the observed trend of the KIE's dependence on the ionic mass.

It is very challenging to experimentally probe which of the competing processes (k_1, k_{-1} or k_2) is primarily responsible for the observed inverse KIEs. It is also challenging to employ more sophisticated theoretical methods to describe the charge transfer reaction systems. While theoretical methods such as flexible microcanonical transition state theory [140] could allow for the inclusion of IVR when calculating the lifetime of a reaction complex, this approach was developed for processes occurring on a single PES. As noted in section 4.3, multiple PESs and non-adiabatic couplings of high dimensionality need to be considered, since the results indicate that the vibrational modes of ammonia play a role. The difficulty of computing such PESs and couplings also limits the possibility of running trajectory calculations to establish theoretical predictions for the relative importance of the competing processes at play. However, based on the features of the PESs, the feasibility of the above mechanism can be discussed.

While the rate coefficient for charge transfer is related to the strength of the coupling

between the PESs, it is difficult to precisely predict the probability of charge transfer based on this property alone. Other factors—such as the width and location of the non-adiabatic coupling, in addition to the shape of the underlying surfaces, their energetic separation, and the collision energy—are also important when considering the likelihood of charge transfer. As depicted in Figure 4.6, for the Ar^+ system, the favourable location of the maximum of the coupling strength near the inner turning point of the one-dimensional entrance-channel potential is (amongst other factors) likely to contribute to faster charge transfer. Hence a larger value for k_2 is predicted in the case of Ar^+.

In summary, the charge transfer reactions appear to be not capture-limited. A mechanism for the electron transfer is proposed, based on the different properties of the reaction complexes and the features of the PESs. The increase in the density of vibrational states for $[Rg–ND_3]^+$ will extend the lifetime of the complex compared to the $[Rg–NH_3]^+$ system, lowering k_{-1} and allowing more time for product formation to occur. That could lead to the observed inverse KIEs. Based on the favourable position of the maximum coupling strength of the Ar^+ system, a larger k_2 value is predicted. This, in turn, decreases the importance of the k_{-1} process resulting in the less-pronounced inverse KIE. This explanation is consistent with the experimentally observed periodic trend. The Ar^+ system displays the lowest inverse KIE (i.e., the KIE is closest to 1), and also features the complexes with the lowest relative densities of states; the $[Xe–ND_3]^+$ complex has the highest density of states, and the Xe^+ system exhibits the highest inverse KIE.

An earlier theory-based study of secondary KIEs broadly supports this proposed explanation. The study found the structure and properties of the transition state

complex determined whether a normal or inverse KIE was expected for a series of S_N2 reactions [141]. From a consideration of the various factors that might contribute to KIEs, the study concluded that the vibrational degrees of freedom of the reaction complex were primarily responsible for any overall inverse KIEs. Note that only comparatively small inverse or normal KIEs were predicted, ranging from 0.9–1.1. While the explanation proposed above could account for the observed periodic trend in the inverse KIE, further experimental and theoretical work is needed to confirm the validity of this theory.

4.5 Implications

As discussed in Chapter 1, only a small fraction of astrochemically interesting processes have been experimentally examined at temperatures below 300 K. As such, to model the chemistry that takes place in the ISM, astrochemical models are necessarily reliant on predictions. Rate coefficients for ion-neutral collisions, such as the charge transfer reactions examined in this chapter, are often derived from capture theory calculations or extrapolated from measurements taken at room temperature.

Both hydrogenated ammonia and fully deuterated ammonia have been observed in the ISM [88]. While the reactions of heavier rare gas ions are not directly relevant to astrochemistry, lighter rare gas ions are prevalent in the ISM. Ar is known to be present in the ISM and Ar^+ is expected to play a role in interstellar chemical reactions [90]. As there are few existing experimental studies of charge transfer reactions with rare gas ions at collision energies < 300 K, their rate coefficients in astrochemical databases are almost entirely based on capture theory calculations. The results presented here indicate that capture theory models consistently over-

estimate the rate coefficients for charge transfer reactions involving rare gas ions and ammonia molecules.

These findings are consistent with previous work on the $He^+ + NH_3$ system (conducted at 300 K), where the experimental rate coefficient was also found to be significantly lower than the ADO capture theory prediction [142]. The $He^+ + NH_3$ system is more chemically complex than the $Xe^+ + NH_3$, $Kr^+ + NH_3$ and $Ar^+ + NH_3$ systems, as charge transfer is not the dominant reaction channel. Not only are other reaction channels open, $NH_2^+ + H + He$ products are preferentially formed. However, an overall experimental rate coefficient for reaction was established for the $He^+ + NH_3$ system, irrespective of what products were formed, facilitating a comparison with capture theories. (Capture theories calculate the probability of a reaction occurring, but they cannot discriminate between the formation of different products in systems where more than one reaction channel is energetically open.) The rate coefficients included in the KIDA database for the $He^+ + NH_3$ system are entirely based on the SC classical capture theory model developed by Su & Chesnavich [6]. The SC model takes into account the dipole moment and polarisability of the neutral species and utilises an empirical formula to yield reaction rate coefficients as a function of temperature. As the SC model over-estimates the experimental $He^+ + NH_3$ reaction rate coefficient at 300 K, it is unlikely to be an appropriate model for describing the low-temperature behaviour of the system.

The results presented in this chapter illustrate that capture theory models are not always accurate at predicting the reaction rate coefficients of ion-molecule reaction systems, even for processes as "simple" as charge transfer. Further work, involving both calculations and experimental measurements, is needed to gain insights into

when capture theory predictions can be confidently utilised. Future work is planned to undertake reactions between Xe^+, Kr^+ and Ar^+ and a supersonically expanded beam of NH_3 or ND_3 neutrals. Only few rotational states (mainly $J = 0$ and 1) will be populated in the ammonia beam. The ACCSA model predicts that the rate coefficient decreases with increasing rotational state population. As such, the proposed experiments—in conjunction with the room-temperature studies detailed here—will further test the validity of capture theory predictions. The charge transfer reactions could be studied under fully state-selected conditions by integrating the linear Paul trap with a Stark decelerator. The decelerator utilises the Stark effect to remove kinetic energy from low-field seeking polar molecules, generating a translationally cold (with tunable velocity range) and state-selected ($J = 1, K = 1$) beam of ammonia molecules. The beam is focused into the ion trap centre, enabling the ammonia to react with the sympathetically cooled rare gas ions. Such experiments will provide fundamental insights in the electron transfer mechanism. Another future project will aim at exciting specific vibrational modes of the NH_3 or ND_3 reactants, such as the ammonia umbrella motion, to probe their influence on the rate coefficient.

In an attempt to further investigate how prevalent inverse KIEs might be in charge transfer reactions between ions and polar molecules, the reactivity of a different neutral polar reactant species has been examined. Chapter 5 details the results from the charge transfer reactions between sympathetically cooled, ground-state Kr^+ ions and H_2O or D_2O neutrals. The results are discussed once more within the framework of capture theories and are compared with the ammonia findings.

Chapter 5

Water charge transfer reactions

To further investigate the prevalence of the effects described in Chapter 4, charge transfer reactions are undertaken with different polar species: H_2O and D_2O (both species observed in the ISM [89]). From the perspective of capture theory models, water and ammonia are predicted to behave in a similar way; they possess a comparable dipole moment and polarisability. Measured reaction rate coefficients are discussed in the context of capture theory models, with the role that they play in describing the behaviour of ion-molecule reactions also explored in more general terms.

5.1 Experimental details

Kr^+ ions have been chosen as the ionic reactant for this study for a number of reasons. In the first instance, the $Xe^+ + H_2O$ system cannot be studied, as the charge transfer reaction channel is endothermic by approximately 0.5 eV. For the $Ar^+ + H_2O$ system, although the charge transfer channel is energetically accessible, the hydrogen abstraction channel is also open [143]. On the contrary, for the $Kr^+ + H_2O$ system, the charge transfer process is the only energetically allowed reaction pathway, with an exothermicity of $\Delta H = -1.38$ eV. Other reaction pathways, such

as hydrogen abstraction $Kr^+ + H_2O \longrightarrow KrH^+ + HO$ ($\Delta H = 0.4\,eV$), are endothermic for the $^2P_{3/2}$ ground-state reactants [144]. This facilitates a straightforward analysis. More importantly, though, Kr^+ provides an interesting comparison study between the different polar species. The ammonia inverse KIE observed for the Kr^+ system falls in between the Xe^+ and Ar^+ cases and the measured rate coefficients are substantially lower than capture theory predictions.

The experimental procedure followed to undertake the water reactions is similar to the one described for the ammonia neutrals. Ground-state, sympathetically cooled Kr^+ ions are produced as described in Chapter 3. H_2O or D_2O vapour at 293 K (from a liquid water reservoir) is admitted to the ion trap via the high-precision leak valve, initiating the reaction. While the laser-cooled Ca^+ ions do not react with ammonia neutrals, they do with water, producing $CaOH^+$ (or $CaOD^+$) ions. This reaction proceeds via the Ca^+ metastable $3d\,^2D_{3/2}$ state, populated in the laser cooling cycle [51]. However, background reaction studies between mono-component Ca^+ Coulomb crystals and water neutrals showed that the rate of this competitive reaction is negligible on the timescale of a charge transfer reaction. Assessed by ToF-MS information, if any $CaOH^+$ or $CaOD^+$ ions are produced, they are included in the analysis and explicitly accounted for.

A further complication that needs to be considered relates to the operation of the heat exchange device. Some amount of water vapour, as it enters the trap chamber through the high-precision leak valve, freezes on the surface of the device. This is evident by the inconsistent ion gauge pressure readings when the cold finger is in operation and water is admitted to the reaction chamber. As such, the reliability of the ion gauge readings (the standard means of monitoring partial pressures in Coulomb

crystal reactions) is compromised in this reaction system. The heat exchange device is, nevertheless, necessary to study the reactions. Without its operation, reactions with background gases present in the chamber take place at an enhanced rate. To overcome this limitation, the high-precision leak valve was carefully calibrated; water vapour was admitted to the chamber at different leak valve settings, with and without N_2 flowing through the heat exchange device. The calibration was complemented by qualitative and quantitative information from the residual gas analyser. In spite of these efforts, the uncertainty with which the water partial pressure can be established is larger compared to the ammonia gas partial pressure uncertainty. Out of an abundance of caution, uncertainties are assigned as one standard deviation of all the calibration measurements taken for each water partial pressure.

As mentioned above, for the $Kr^+ + H_2O$ system, the charge transfer process is the only energetically allowed reaction pathway, with $\Delta H = -1.38\,\text{eV}$. ToF-MS data confirm the absence of any competitive reaction channels for both the hydrogenated and deuterated reaction systems. Reactions with background species are either absent or negligible (and are specifically taken into account in the analysis, when present). The trapping depths experienced by the ionic species involved in the charge transfer reactions (calculated using equation 3.1) are 2.9 eV for Ca^+, 1.1 eV for Kr^+, 7.1 eV for H_2O^+ and 6.4 eV for D_2O^+. Hence, all ions of interest are efficiently trapped and the reactions can be considered one-to-one processes. Rate coefficients are calculated as detailed in Chapter 3 and are summarised in Table 5.1. Note that rate coefficients obtained by the linear correlation method are included here for reference, however, as with the ammonia reactions, they are not used further.

Table 5.1: Pseudo-first order (in ($\times 10^{-2}$ s^{-1})), k', and bimolecular rate coefficients (in $\times 10^{-9}$ $cm^3\,s^{-1}$) calculated for the reaction systems of interest using the average, k, and linear correlation, k_{lin}, methods. The number of points and weighted temperatures of each reaction system are also included.

Reaction system	k'	k	k_{lin}	No. of Points	T (K)
$Kr^+ + H_2O$	3.3(4)	1.8(7)	1.7(2)	10	244
$Kr^+ + D_2O$	2.8(2)	2(1)	1.1(2)	7	240

5.2 Results

The ADO and ACCSA models are again employed for comparison with the experimentally measured rate coefficients. The ACCSA model, although developed for symmetric top molecules, can be used to predict the rate coefficients of asymmetric top reactants, such as H_2O or D_2O. At temperatures below 300 K, the neutrals can be approximated as prolate symmetric tops, as the K quantum numbers (the projection of j onto the molecular-fixed axis) are not expected to have a significant effect on the reaction rate coefficients [25]. With this approximation, the asymmetric top rotational constants B and C are averaged to obtain a symmetric constant B'. ACCSA rate coefficients can also be calculated using the relevant asymmetric top equations. A comparison study between the symmetric top approximation and the asymmetric top approach found that the reaction rate coefficients calculated using each approach do not differ significantly [145]. Given the above, and considering that the water charge transfer reactions are undertaken at temperatures that range between 240–244 K, ACCSA rate coefficients are calculated using the symmetric top model detailed in Appendix A. Table 5.2 summarises the parameters used in the capture theory calculations.

Table 5.2: Polarisabilities, dipole moments [146], c parameters, and rotational constants A and B' used to calculate the capture theory rate coefficients. The rotational constants B' are an average of the H_2O or D_2O rotational constants B and C [123].

Isotopologue	α (cm^3)	μ_D (D)	c	A (cm^{-1})	B' (cm^{-1})
H_2O	1.45×10^{-24}	1.848	0.254	27.877	11.899
D_2O	1.44×10^{-24}	1.851	0.254	15.420	6.059

Table 5.3 and Figure 5.1 summarise the experimental rate coefficients established for the $Kr^+ + H_2O$ and $Kr^+ + D_2O$ reaction systems as well as the predictions from the ADO and ACCSA models. The relative magnitudes of the experimental rate coefficients suggest that no KIE is observed, with $k_H/k_D = 0.9(6)$. Additionally, the experimental results are in very good agreement with the classical ADO predictions. As the reactions are studied under conditions that can still be considered classical, this agreement indicates that the electron transfer follows a capture-limited mechanism. Note that, although the uncertainties are larger than those stated for the ammonia reactions (see above), the reported values of the rate coefficients are very similar and fall right on top of the ADO predictions.

Table 5.3: Experimental, ADO and ACCSA rate coefficients (in $cm^3\,s^{-1} \times 10^{-9}$) for the charge transfer reactions between Kr^+ ions and the two water isotopologues of interest.

Reaction system	k_{exp}	k_H/k_D	k_{ADO}	k_{ACCSA}	T (K)
$Kr^+ + H_2O$	1.8(7)		1.98	2.98	244
$Kr^+ + D_2O$	2(1)	0.9(6)	1.90	2.91	240

The $Kr^+ + H_2O$ system has been studied previously at 296 K using the flowing afterglow technique. A rate coefficient of $k = 1.2(2) \times 10^{-9}\,cm^3\,s^{-1}$ was reported [143].

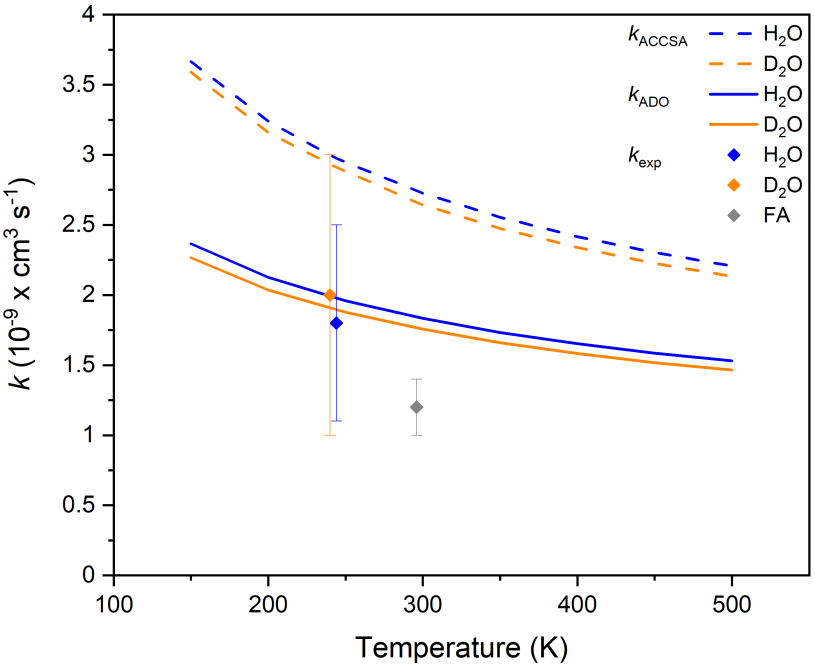


Figure 5.1: Charge transfer rate coefficients for the $Kr^+ + H_2O$ (blue) and $Kr^+ + D_2O$ (orange) reaction systems, as established from capture theory models (ACCSA and ADO) and from experimental measurements. Previous work conducted at 296 K is included for comparison (grey) [143]. Error bars indicate the uncertainty in the experimental rate coefficients (see section 3.4 and previous work [143]).

It is unclear if the Kr^+ ions were state-selected, or if both $^2P_{3/2}$ and $^2P_{1/2}$ electronic states were populated during the reactions. Additionally, flowing afterglow experiments are undertaken under very different conditions compared to those adopted in this work (at pressures many orders of magnitude higher). As such, these results are not directly comparable with the rate coefficients measured here.

Interestingly, the inverse KIE behaviour detailed in Chapter 4 for the ammonia charge transfer reactions is not observed in the water systems. For the Rg^+ + am-

monia systems, electron transfer is evidently not capture-limited and an inverse KIE is observed, whilst the Kr^+ + water reactions appear to follow a capture mechanism, with no isotope effect recorded. For processes that are not capture limited, competition between the magnitude of k_2 (the rate of charge transfer) and k_{-1} (dissociation back to products) is expected. As speculated in section 4.4, the inverse KIEs observed in the ammonia + rare gas reaction systems could arise from differences in the properties of the hydrogenated and deuterated reaction complexes, such as their lifetimes, that alter the relative magnitudes of k_{-1}. Conversely, for a reaction that follows a capture mechanism (with $k_2 >> k_1 > k_{-1}$), the properties of the complex will not play such an important role, as reactions occur at a much faster rate after complex formation. As such, the water charge transfer systems appear to be capture limited and no KIE is observed.

Theoretical work on the Kr^+ + H_2O reaction system is currently in progress. In contrast to the ammonia reactions, where no energetically-accessible crossing points were identified between the reactant and product PESs, such a crossing is anticipated for the capture-limited water reactions. It is expected that, in the near future, theory will aid the understanding of the experimental results presented in this chapter and further elucidate the different findings seen in the water and ammonia charge transfer systems.

5.3 Implications

Capture theories have been found to successfully describe the behaviour of a number of ion-molecule reactions. For example, the N^+ + H_2O and N^+ + NH_3 reaction systems, studied in CRESU and SIFT experiments, show good agreement with the

ACCSA [118] and ADO or empirical SC models [2]. As such, capture theories have been widely utilised in astrochemical models to estimate rate coefficients of experimentally unmeasured reactions [18].

Water and ammonia possess a comparable dipole moment and polarisability and, as such, they are predicted to behave in a similar way within the context of capture theory models. However, the charge transfer reactions studied in this thesis demonstrate that capture theories are not always accurate at predicting reaction rate coefficients, even at energies near 300 K. Other ion-molecule reactions, undertaken within the highly controlled and cold environment of Coulomb crystals, have reported rate coefficients that are also inconsistent with capture theory models. For example, a study between laser-cooled Be^+ ions in their ground state and room-temperature H_2O, at an effective reaction temperature of 100 K, reported an experimental rate coefficient that was only half the magnitude predicted by ADO calculations. As established from trajectory calculations, the effect was attributed to the presence of a submerged barrier along the reaction pathway [46]. The presence (and, in particular, the height) of a submerged barrier is known to influence the agreement between experimental rate coefficients and capture theory predictions, as previously demonstrated for reactions between laser-cooled Ca^+ ions and velocity-selected CH_3F and CH_3Cl neutrals [10].

On the contrary, the different reactivities of sympathetically cooled N_2H^+ ions with ortho- and para-water (separated by an electrostatic deflector) were successfully explained within the framework of state-selected, rotationally adiabatic quantum capture theory [63]. The astrochemically interesting reaction between sympathetically cooled CCl^+ and thermal CH_3CN neutrals, at an effective reaction temperature

of 160 K, was also found to be in good agreement with ADO predictions [59]. Similarly, Langevin predictions successfully described reactions between sympathetically cooled CCl^+ and C_2H_2 neutrals [58].

The charge transfer reactions between sympathetically cooled O_2^+ or N_2^+ and ground- or excited-state Rb atoms, examined in a hybrid ion-neutral trap, reported an interplay between short- and long-range interactions that depend on the quantum state of the reactants. Based on *ab initio* calculations, the strength of the non-adiabatic coupling was shown to govern these effects and, subsequently, the agreement between the experimental findings and classical capture theory predictions. Interestingly, the study concluded that without the aid of high-level calculations, it is not straightforward to predict the behaviour of the different charge transfer systems [71].

The few examples given above, together with the ammonia and water findings presented as part of this work, show that capture theories do not consistently agree with reaction studies undertaken within Coulomb crystals, at a range of temperatures (from state-selected reactions to systems with a classical distribution of rotational states at energies near 300 K). Rate coefficients measured with other experimental techniques can also deviate from capture theory predictions, as seen in the NH_3 charge transfer reactions with rare gas ions at 300 K in ICR and SIFT experiments [110, 124, 142]. The $O^+ + N_2$ reaction, studied using the CRESU technique, was also found to exhibit a rate coefficient two orders of magnitude below the Langevin theory prediction [147]. As noted in Chapter 4, the inverse KIEs observed for the ammonia charge transfer reactions cannot be rationalised within the framework of capture theories.

To model the rich chemistry that takes place in the ISM, capture theory models are a useful tool. There is a lack of experimental data recorded under relevant conditions, and capture theory predictions provide computationally straightforward predictions of reaction rate coefficients. This has seen their widespread adoption in astrochemical databases such as KIDA. However, as the work of this thesis highlights, it is exceedingly challenging to predict whether a selected reaction follows a capture mechanism in the absence of supporting experimental data or high-level *ab initio* calculations. Hence, the validity of capture theory needs to be considered in each individual reaction system, either via experimental or theoretical means. The need for further work is apparent.

Chapter 6

Conclusions

Undertaking reaction studies within the confines of Coulomb crystals, trapped in linear Paul traps, is increasingly being recognised as a powerful method for studying ion-molecule reactions. The combination of trapping and laser cooling techniques allow reactions to be examined with exceedingly high sensitivity, in nearly perturbation-free conditions. The versatile sympathetic cooling technique allows the incorporation of many ionic species in the Coulomb crystal framework and, as such, their use in reaction studies. Here, the charge transfer reactions between sympathetically cooled, rare gas Xe^+, Kr^+ or Ar^+ ions and thermal ammonia and water molecules are investigated. Both the fully hydrogenated and fully deuterated molecular analogues are employed. MD simulations, complemented by ToF-MS information, allow the determination of reaction rate coefficients. The reactions are undertaken at lower than 300 K collision energies, spanning 194–260 K. All molecules used in this study (NH_3, ND_3, H_2O and D_2O) have been observed in the ISM. Light rare gas ions, such as Ar^+, are also present in the ISM and are expected to play a role in the chemistry of these environments.

A number of interesting effects are reported for the ammonia charge transfer reactions. Inverse KIEs are observed for the three reaction systems studied, with the magnitude of the effect showing a dependence on the mass of the ionic species;

$k_H/k_D = 0.30(5)$ for the heaviest Xe^+ reaction systems, while $k_H/k_D = 0.8(3)$ for the lightest Ar^+ systems. The magnitude of the inverse KIE falls in between for the Kr^+ ions ($k_H/k_D = 0.5(2)$). As secondary KIEs usually range between $k_H/k_D = 1.2-0.8$, the observed effects for the Xe^+ and Kr^+ systems are notably pronounced. Capture theories fail to describe the behaviour of these reactions, predicting only a small normal KIE. Further, the experimentally measured rates coefficients are suppressed in comparison to capture theory predictions (calculated using both a classical and a quantum capture model).

With the aid of high-level *ab initio* calculations and an one-dimensional QM model, an explanation for these findings is proposed. No energetically accessible curve crossing is identified in the constructed PESs, suggesting that the electron transfer mechanism is not straightforward. The ammonia charge transfer reactions are evidently not capture-limited. It is speculated that properties of the reaction complex (such as its lifetime) will play a role in the probability of product formation. The predicted longer lifetime of the deuterated reaction complex, $[Rg–ND_3]^+$, could give rise to the observed inverse KIEs, while the trend in the magnitude of the effects is rationalised based on the position of the maximum of the non-adiabatic couplings. The favourable position of the coupling in the Ar^+ reaction system is speculated to lead to an increased rate of charge transfer within the reaction complex, which in turn results in a less pronounced inverse KIE. Further work, involving additional experiments and theoretical investigations, is needed to confirm this tentative explanation.

In a bid to probe the prevalence of these effects in other systems, reactions were undertaken between sympathetically cooled Kr^+ ions and water isotopologues. Inter-

estingly, the rate coefficients measured for the water systems are in good agreement with classical capture theory predictions and no KIE is observed. Theoretical work, currently in progress, is expected to confirm these findings.

Given the lack of experimental data relevant to the ISM chemistry, capture theories are often employed in astrochemical models to provide an estimate of rate coefficients of unmeasured ion-molecule reactions. This lack of experimental studies is also evident when considering deuterated species, even though D-substituted molecules are known to be abundant in the ISM. The findings of this thesis indicate that capture theories are not always accurate at predicting the behaviour of ion-molecule systems, even for seemingly "simple" charge transfer reactions. Note that water and ammonia possess a comparable dipole moment and polarisability and would be expected to behave in a similar way (when examined within the framework of capture theory). Further, the disagreement between the experimental findings and capture theory calculations at energies near 300 K suggests that capture theory models are unlikely to predict the behaviour of such systems at the low temperatures prevalent in the ISM.

Following the publication of the findings described in Chapter 3 and 4 of this thesis, further evidence of inverse KIEs has been reported for reactions between sympathetically cooled CCl^+ and CH_3CN neutrals [59]. The reactions were also undertaken within the environment of Ca^+ Coulomb crystals, under conditions comparable to the charge transfer reaction detailed in this work. The observation of inverse KIEs in systems beyond what is reported in this thesis illustrate that inverse KIEs effects may be present in a number of different systems. Clearly, the presence (or absence) of isotope effects warrant further attention. More work is needed to fully unravel

the mechanisms that give rise to the observed findings. Proposed experiments to further probe the ammonia reactions as a function of temperature, by employing a beam of ammonia neutrals with a low rotational state distribution (and tunable velocity), are discussed in Chapter 4. Additionally, a cryogenic linear Paul trap is currently under development in the Liverpool lab. This apparatus will be used in future experiments to study reactions under truly cold conditions, shedding more light on ion-molecule reaction mechanisms.

Appendix A

ACCSA rate coefficients

Following the method proposed by D. Clary [118], the ACCSA rate coefficients are calculated using

$$k_{\mathrm{ACCSA}} = \frac{\sum\limits_{jK} g_{jK} \exp\left[-E_{jK}/(k_B T)\right] k_{jK}(T)}{\sum\limits_{jK} g_{jK} \exp\left[-E_{jK}/(k_B T)\right]}, \tag{A.1}$$

where g_{jK} is the degeneracy factor, E_{jK} the barrier height of the potential curve and k_{jK} the rate coefficient for each rotational state (j, K). Table A.1 summarises the g_{jK} factors for symmetric top molecules, such as the ammonia, as a function of the rotational state K [145].

Table A.1: Degeneracy factors, g_{jK}, as a function of K. If K is divisible by 3, g_{jK} = 4, otherwise g_{jK} = 2.

K	0	1	2	3	...	$K \not\equiv 0 \pmod 3$	$K \equiv 0 \pmod 3$
g_{jK}	1	2	2	4	...	2	4

Rate coefficients for individual rotational states, k_{jK}, are calculated using the equation

$$k_{jK}(T) = \sqrt{\frac{8}{\pi\mu(k_B T)^3}} \int_0^\infty \sigma(j, K, E) E \exp[-E/(k_B T)] dE, \tag{A.2}$$

where E is the collision energy and $\sigma(j, K, E)$ the reaction cross section. The latter

is calculated by

$$\bar{\sigma}(j,K,E) = \frac{\pi}{k^2(2j+1)} \sum_{\Omega} \left[J_{\max}(j,K,\Omega)+1\right]^2, \tag{A.3}$$

where $k^2 = 2\mu E/\hbar^2$ and $J_{\max}(j,K,\Omega)$ is the maximum angular momentum for which the collision energy is greater than the maximum potential ($E \geq V_{J_{jK\Omega}}(R)$). To obtain the potential curves, $V_{J_{jK\Omega}}(R)$, one can use

$$V_{JjK\Omega}(R) = \varepsilon_{jK\Omega}(R) + \frac{\hbar^2 J(J+1)}{2\mu R^2} - E_{jK}, \tag{A.4}$$

where $\varepsilon_{jK\Omega}$ is the adiabatic potential and $E_{jK} = Bj(j+1) + (A-B)K^2$. The rotational constants A and B are 6.19600 cm^{-1} and 9.44430 cm^{-1} for NH_3; 3.14420 cm^{-1} and 5.14280 cm^{-1} for ND_3 [123]. $\varepsilon_{jK\Omega}(R)$ is calculated by diagonalisation of the coupling matrices $V_{jj'}$ as a function of the distance R between the ammonia and the rare gas ion. It is given by

$$V_{jj'} = \left\{ E_{jK} + \frac{\left[j(j+1)\hbar^2 - 2\Omega^2\hbar^2\right]}{2\mu R^2} - \frac{\alpha q^2}{2R^4} \right\} \delta_{ji'} - \frac{q\mu_D \left\{ C \begin{pmatrix} j & j' & 1 \\ -K & K & 0 \end{pmatrix} C \begin{pmatrix} j & j' & 1 \\ -\Omega & \Omega & 0 \end{pmatrix} \left[(2j+1)\,(2j'+1)\right]^{1/2} \right\}}{3R^2}. \tag{A.5}$$

C are the Clebsch-Gordon coefficients. Note that a matrix size of 201×201 is used for the coupling matrices. The distance between the coupling elements ranges from 1.5 Å to 55 Å with an interval of 0.05 Å.

The same method is used for the calculation of the water ACCSA rate coefficients. The neutral is treated as a symmetric top with degeneracy factors

K	0	1	2	3	...	$K \not\equiv 0 \pmod 2$	$K \equiv 0 \pmod 2$
g_{jK}	1	6	2	6	...	6	2

and rotational constants $A = 27.877\,\mathrm{cm}^{-1}$ and $B' = 11.899\,\mathrm{cm}^{-1}$ for H_2O; $15.420\,\mathrm{cm}^{-1}$ and $6.059\,\mathrm{cm}^{-1}$ for D_2O [123] (B' is taken as the average of the asymmetric rotational constants B and C, as detailed in Chapter 5).

Bibliography

[1] D. C. Clary. *Annu. Rev. Phys. Chem.*, **41**, 61, 1990.

[2] J. B. Marquette, B. R. Rowe, G. Dupeyrat, G. Poissant, and C. Rebrion. *Chem. Phys. Lett.*, **122**, 431, 1985.

[3] M. P. Langevin. In *Annales de Chimie et de Physique, Series*, volume **5**, 245, 1905.

[4] G. Gioumousis and D. P. Stevenson. *J. Chem. Phys.*, **29**, 294, 1958.

[5] T. Su and M. T. Bowers. *J. Chem. Phys.*, **58**, 3027, 1973.

[6] T. Su and W. J. Chesnavich. *J. Chem. Phys.*, **76**, 5183, 1982.

[7] D. C. Clary. *J. Chem. Soc., Faraday Trans. 2*, **83**, 139, 1987.

[8] J. Troe. *J. Chem. Phys.*, **87**, 2773, 1987.

[9] B. R. Heazlewood and T. P. Softley. *Nat. Rev. Chem.*, **5**, 125, 2021.

[10] A. D. Gingell, M. T. Bell, J. M. Oldham, T. P. Softley, and J. N. Harvey. *J. Chem. Phys.*, **133**, 194302, 2010.

[11] B. A. McGuire. *Astrophys. J. Suppl. Ser.*, **239**, 17, 2018.

[12] T. Albertsson, D. A. Semenov, A. I. Vasyunin, T. Henning, and E. Herbst. *Astrophys. J. Suppl. Ser.*, **207**, 27, 2013.

[13] I. W. M. Smith. *Annu. Rev. Astron. Astrophys.*, **49**, 29, 2011.

[14] I. R. Cooke and I. R. Sims. *ACS Earth Space Chem.*, **3**, 1109, 2019.

[15] V. Wakelam, E. Herbst, J. C. Loison, I. W. M. Smith, V. Chandrasekaran, B. Pavone, N. G. Adams, M. C. Bacchus-Montabonel, A. Bergeat, K. Béroff, et al. *Astrophys. J. Suppl. Ser.*, **199**, 21, 2012.

[16] F. Le Petit, C. Nehmé, J. Le Bourlot, and E. Roueff. *Astrophys. J. Suppl. Ser.*, **164**, 506, 2006.

[17] D. McElroy, C. Walsh, A. J. Markwick, M. A. Cordiner, K. Smith, and T. J. Millar. *Astron. Astrophys.*, **550**, A36, 2013.

[18] V. Wakelam, I. W. M. Smith, E. Herbst, J. Troe, W. Geppert, H. Linnartz, K. Öberg, E. Roueff, M. Agúndez, P. Pernot, et al. *Space Sci. Rev.*, **156**, 13, 2010.

[19] D. Gerlich and S. Schlemmer. *Planet. Space Sci.*, **50**, 1287, 2002.

[20] S. Schlemmer, O. Asvany, E. Hugo, and D. Gerlich. *Proc. Int. Astron. Union*, **1**, 125, 2005.

[21] H. Roberts, E. Herbst, and T. J. Millar. *Astron. Astrophys.*, **424**, 905, 2004.

[22] F. C. Fehsenfeld, A. L. Schmeltekopf, P. D. Goldan, H. I. Schiff, and E. E. Ferguson. *J. Chem. Phys.*, **44**, 4087, 1966.

[23] N. G. Adams and D. Smith. *Int. J. Mass Spectrom. and Ion Physics*, **21**, 349, 1976.

[24] D. Smith, P. Spanel, and C. A. Mayhew. *Int. J. Mass Spectrom. Ion Processes*, **117**, 457, 1992.

[25] D. C. Clary, D. Smith, and N. G. Adams. *Chem. Phys. Lett.*, **119**, 320, 1985.

[26] S. G. Ard, A. A. Viggiano, and N. S. Shuman. *J. Phys. Chem. A*, **125**, 3503, 2021.

[27] G. Dupeyrat, J. B. Marquette, and B. R. Rowe. *Phys. Fluids*, **28**, 1273, 1985.

[28] M. Fournier, S. D. Le Picard, and I. R. Sims. In *Cold Chemistry: Molecular Scattering and Reactivity Near Absolute Zero*, pages 1–45. The Royal Society of Chemistry, 2018.

[29] B. R. Rowe and J. B. Marquette. *Int. J. Mass Spectrom. Ion Processes*, **80**, 239, 1987.

[30] I. W. M. Smith and B. R. Rowe. *Acc. Chem. Res.*, **33**, 261, 2000.

[31] C. Rebrion, B. R. Rowe, and J. B. Marquette. *J. Chem. Phys.*, **91**, 6142, 1989.

[32] T. Speck, T. I. Mostefaoui, D. Travers, and B. R. Rowe. *Int. J. Mass Spectrom.*, **208**, 73, 2001.

[33] W. T. Huntress Jr. *Astrophys. J. Suppl. Ser.*, **33**, 495, 1977.

[34] G. Mauclaire, R. Derai, S. Fenistein, and R. Marx. *J. Chem. Phys*, **70**, 4017, 1979.

[35] D. Gerlich. *Phys. Scr.*, **1995**, 256, 1995.

[36] R. Plasil, T. Mehner, P. Dohnal, T. Kotrik, J. Glosik, and D. Gerlich. *Astrophys. J.*, **737**, 60, 2011.

[37] R. Wester. *J. Phys. B: At. Mol. Opt. Phys.*, **42**, 154001, 2009.

[38] M. Nötzold, S. Z. Hassan, J. Tauch, E. Endres, R. Wester, and M. Weidemüller. *Appl. Sci.*, **10**, 5264, 2020.

[39] M. Germann, X. Tong, and S. Willitsch. *Nat. Phys.*, **10**, 820, 2014.

[40] B. R. Heazlewood. *Mol. Phys.*, **117**, 1934, 2019.

[41] P. F. Staanum, K. Højbjerre, R. Wester, and M. Drewsen. *Phys. Rev. Lett.*, **100**, 243003, 2008.

[42] M. Drewsen, L. Hornekær, N. Kjærgaard, K. Mølhave, A-M Thommesen, Z. Videsen, A. Mortensen, and F. Jensen. In *AIP Conference Proceedings*, volume **606**, 135. American Institute of Physics, 2002.

[43] K. A. E. Meyer, L. L. Pollum, L. S. Petralia, A. Tauschinsky, C. J. Rennick, T. P. Softley, and B. R. Heazlewood. *J. Phys. Chem. A*, **119**, 12449, 2015.

[44] K. Mølhave and M. Drewsen. *Phys. Rev. A*, **62**, 011401, 2000.

[45] B. Roth, P. Blythe, H. Wenz, H. Daerr, and S. Schiller. *Phys. Rev. A*, **73**, 042712, 2006.

[46] T. Yang, A. Li, G. K. Chen, C. Xie, A. G. Suits, W. C. Campbell, H. Guo, and E. R. Hudson. *J. Phys. Chem. Lett.*, **9**, 3555, 2018.

[47] G. K. Chen, C. Xie, T. Yang, A. Li, A. G. Suits, E. R. Hudson, W. C. Campbell, and H. Guo. *Phys. Chem. Chem. Phys.*, **21**, 14005, 2019.

[48] J. Greenberg, P. C. Schmid, M. Miller, J. F. Stanton, and H. J. Lewandowski. *Phys. Rev. A*, **98**, 032702, 2018.

[49] P. C. Schmid, M. I. Miller, J. Greenberg, T. L. Nguyen, J. F. Stanton, and H. J. Lewandowski. *Mol. Phys.*, **117**, 3036, 2019.

[50] N. Kimura, K. Okada, T. Takayanagi, M. Wada, S. Ohtani, and H. A. Schuessler. *Phys. Rev. A*, **83**, 033422, 2011.

[51] K. Okada, M. Wada, L. Boesten, T. Nakamura, I. Katayama, and S. Ohtani. *J. Phys. B: At. Mol. Opt. Phys.*, **36**, 33, 2002.

[52] B. Roth, D. Offenberg, C. B. Zhang, and S. Schiller. *Phys. Rev. A*, **78**, 042709, 2008.

[53] M. V. DePalatis and M. S. Chapman. *Phys. Rev. A*, **88**, 023403, 2013.

[54] P. Puri, M. Mills, C. Schneider, I. Simbotin, J. A. Montgomery, R. Côté, A. G. Suits, and E. R. Hudson. *Science*, **357**, 1370, 2017.

[55] M. Fan, C. A. Holliman, X. Shi, H. Zhang, M. W. Straus, X. Li, S. W. Buechele, and A. M. Jayich. *Phys. Rev. Lett.*, **126**, 023002, 2021.

[56] P. C. Schmid, J. Greenberg, T. L. Nguyen, J. H. Thorpe, K. J. Catani, O. A. Krohn, M. I. Miller, J. F. Stanton, and H. J. Lewandowski. *Phys. Chem. Chem. Phys.*, **22**, 20303, 2020.

[57] J. Greenberg, P. C. Schmid, J. H. Thorpe, T. L. Nguyen, K. J. Catani, O. A. Krohn, M. I. Miller, J. F. Stanton, and H. J. Lewandowski. *J. Chem. Phys.*, **154**, 124310, 2021.

[58] K. J. Catani, J. Greenberg, B. V. Saarel, and H. J. Lewandowski. *J. Chem. Phys.*, **152**, 234310, 2020.

[59] O. A. Krohn, K. J. Catani, J. Greenberg, S. P. Sundar, G. da Silva, and H. J. Lewandowski. *J. Chem. Phys.*, **154**, 074305, 2021.

[60] K. Okada, T. Suganuma, T. Furukawa, T. Takayanagi, M. Wada, and H. A. Schuessler. *Phys. Rev. A*, **87**, 043427, 2013.

[61] Y-P Chang, K. Długołęcki, J. Küpper, D. Rösch, D. Wild, and S. Willitsch. *Science*, **342**, 98, 2013.

[62] D. Rösch, S. Willitsch, Y-P Chang, and J. Küpper. *J. Chem. Phys.*, **140**, 03B624, 2014.

[63] A. Kilaj, H. Gao, D. Rösch, U. Rivero, J. Küpper, and S. Willitsch. *Nat. Commun.*, **9**, 1, 2018.

[64] T. Yang, A. Li, G. K. Chen, Q. Yao, A. G. Suits, H. Guo, E. R. Hudson, and W. C. Campbell. *Sci. Adv.*, **7**, eabe4080, 2021.

[65] H. L. Bethlem, G. Berden, and G. Meijer. *Phys. Rev. Lett.*, **83**, 1558, 1999.

[66] N. Vanhaecke, U. Meier, M. Andrist, B. H. Meier, and F. Merkt. *Phys. Rev. A*, **75**, 031402, 2007.

[67] E. Narevicius, A. Libson, C. G. Parthey, I. Chavez, J. Narevicius, U. Even, and M. G. Raizen. *Phys. Rev. Lett.*, **100**, 093003, 2008.

[68] A. Härter and J. Hecker Denschlag. *Contemp. Phys.*, **55**, 33, 2014.

[69] F. H. J. Hall, M. Aymar, M. Raoult, O. Dulieu, and S. Willitsch. *Mol. Phys.*, **111**, 1683, 2013.

[70] W. G. Rellergert, S. .T Sullivan, S. Kotochigova, A. Petrov, K. Chen, S. J. Schowalter, and E. R. Hudson. *Phys. Rev. Lett.*, **107**, 243201, 2011.

[71] A. D. Dörfler, P. Eberle, D. Koner, M. Tomza, M. Meuwly, and S. Willitsch. *Nat. Commun.*, **10**, 1, 2019.

[72] N. Deb, B. R. Heazlewood, M. T. Bell, and T. P. Softley. *Phys. Chem. Chem. Phys.*, **15**, 14270, 2013.

[73] M. Schwarz, O. O. Versolato, A. Windberger, Brunner, et al. *Rev. Sci. Instrum.*, **83**, 083115, 2012.

[74] M. Hejduk and B. R. Heazlewood. *Rev. Sci. Instrum.*, **90**, 123701, 2019.

[75] S. E. Barlow, J. A. Luine, and G. H. Dunn. *Int. J. Mass Spectrom. Ion Processes*, **74**, 97, 1986.

[76] M. M. Schauer, S. R. Jefferts, S. E. Barlow, and G. H. Dunn. *J. Chem. Phys.*, **91**, 4593, 1989.

[77] R. C. Thompson, S. Donnellan, D. R. Crick, and D. M. Segal. *J. Phys. B: At. Mol. Opt. Phys.*, **42**, 154003, 2009.

[78] A. P. O'Connor, X. Urbain, J. Stützel, K. A. Miller, N. de Ruette, M. Garrido, and D. W. Savin. *Astrophys. J. Suppl. Ser.*, **219**, 6, 2015.

[79] P-M Hillenbrand, K. P. Bowen, F. Dayou, K. A. Miller, N. de Ruette, X. Urbain, and D. W. Savin. *Phys. Chem. Chem. Phys.*, **22**, 27364, 2020.

[80] K. P. Bowen, P-M Hillenbrand, J. Liévin, D. W. Savin, and X. Urbain. *J. Chem. Phys.*, **154**, 084307, 2021.

[81] P. Allmendinger, J. Deiglmayr, K. Höveler, O. Schullian, and F. Merkt. *J. Chem. Phys.*, **145**, 244316, 2016.

[82] V. Zhelyazkova, F. B. V. Martins, J. A. Agner, H. Schmutz, and F. Merkt. *Phys. Rev. Lett.*, **125**, 263401, 2020.

[83] L. Pan and D. R. Beck. *Phys. Rev. A*, **82**, 014501, 2010.

[84] C. W. Walter, N. D. Gibson, Y-G Li, D. J. Matyas, R. M. Alton, S. E. Lou, R. L. Field III, D. Hanstorp, L. Pan, and D. R. Beck. *Phys. Rev. A*, **84**, 032514, 2011.

[85] P. Yzombard, M. Hamamda, S. Gerber, M. Doser, and D. Comparat. *Phys. Rev. Lett.*, **114**, 213001, 2015.

[86] B. P. Mant, F. A. Gianturco, R. Wester, E. Yurtsever, and L. González-Sánchez. *Phys. Rev. A*, **102**, 062810, 2020.

[87] M. R. Tarbutt. *Contemp. Phys.*, 2019.

[88] D. C. Lis, E. Roueff, M. Gerin, T. G. Phillips, L. H. Coudert, F. F. S. Van Der Tak, and P. Schilke. *Astrophys. J. Lett.*, **571**, L55, 2002.

[89] H. M. Butner, S. B. Charnley, C. Ceccarelli, S. D. Rodgers, J. R. Pardo, B. Parise, J. Cernicharo, and G. R. Davis. *Astrophys. J. Lett.*, **659**, L137, 2007.

[90] P. Schilke, D. A. Neufeld, H. S. P. Müller, C. Comito, E. A. Bergin, D. C. Lis, M. Gerin, J. H. Black, M. Wolfire, N. Indriolo, et al. *Astron. Astrophys.*, **566**, A29, 2014.

[91] W. Paul. *Angew. Chem. Int. Ed. Engl.*, **29**, 739, 1990.

[92] M. Drewsen, I. Jensen, J. Lindballe, N. Nissen, R. Martinussen, A. Mortensen, P. Staanum, and D. Voigt. *Int. J. Mass Spectrom.*, **229**, 83, 2003.

[93] C. S. Adams and E. Riis. *Prog. Quantum Electron.*, **21**, 1, 1997.

[94] D. Leibfried, R. Blatt, C. Monroe, and D. Wineland. *Rev. Mod. Phys.*, **75**, 281, 2003.

[95] W. D. Phillips. *Rev. Mod. Phys.*, **70**, 721, 1998.

[96] S. Chu. *Rev. Mod. Phys.*, **70**, 685, 1998.

[97] J. Dalibard and C. Cohen-Tannoudji. *J. Opt. Soc. Am. B*, **6**, 2023, 1989.

[98] S. Willitsch, M. T. Bell, A. D. Gingell, and T. P. Softley. *Phys. Chem. Chem. Phys.*, **10**, 7200, 2008.

[99] E. Wigner. *Phys. Rev.*, **46**, 1002, 1934.

[100] D. H. .E Dubin and T. M. O'neil. *Rev. Mod. Phys.*, **71**, 87, 1999.

[101] D. J. Wineland, J. C. Bergquist, W. M. Itano, J. J. Bollinger, and C. H. Manney. *Phys. Rev. Lett.*, **59**, 2935, 1987.

[102] E. L. Pollock and J-P Hansen. *Phys. Rev. A*, **8**, 3110, 1973.

[103] B. R. Heazlewood and T. P. Softley. *Annu. Rev. Phys. Chem.*, **66**, 475, 2015.

[104] D. J. Larson, J. C. Bergquist, J. J. Bollinger, W. M. Itano, and D. J. Wineland. *Phys. Rev. Lett.*, **57**, 70, 1986.

[105] T. Baba and I. Waki. *Jpn. J. Appl. Phys.*, **35**, L1134, 1996.

[106] S. J. Bajic, R. N. Compton, X. Tang, and P. Lambropoulos. *Phys. Rev. A*, **44**, 2102, 1991.

[107] S. Jullien, J. Lemaire, S. Fenistein, M. Heninger, G. Mauclaire, and R. Marx. *Chem. Phys. Lett.*, **212**, 340, 1993.

[108] M. Schweizer, S. Mark, and D. Gerlich. *Int. J. Mass Spectrom. Ion Processes*, **135**, 1, 1994.

[109] D. J. Levandier and Y-H Chiu. *J. Chem. Phys.*, **133**, 154304, 2010.

[110] R. Derai, G. Mauclaire, and R. Marx. *Chem. Phys. Lett.*, **86**, 275, 1982.

[111] P. R. Kemper, M. T. Bowers, D. C. Parent, G. Mauclaire, R. Derai, and R. Marx. *J. Chem. Phys.*, **79**, 160, 1983.

[112] A. Viel, W. Eisfeld, S. Neumann, W. Domcke, and U. Manthe. *J. Chem. Phys.*, **124**, 214306, 2006.

[113] A. Tsikritea, K. Park, P. Bertier, J. Loreau, T. P. Softley, and B. R. Heazlewood. *Chem. Sci.*, **12**, 10005, 2021.

[114] N. Deb. *DPhil Thesis, University of Oxford*, 2014.

[115] C. B. Zhang, D. Offenberg, B. Roth, M. A. Wilson, and S. Schiller. *Phys. Rev. A*, **76**, 012719, 2007.

[116] F. Cascarini. *Part II (M. Chem.) Thesis, Universtiy of Oxford*, 2016.

[117] T. Su and M. T. Bowers. *Int. J. Mass Spectrom. Ion Processes*, **17**, 211, 1975.

[118] D. C. Clary. *Mol. Phys.*, **54**, 605, 1985.

[119] K. Park. *Part II (M. Chem.) Thesis, University of Oxford*, 2020.

[120] R. L. Woodin and J. L. Beauchamp. *J. Am. Chem. Soc.*, **100**, 501, 1978.

[121] E. A. Halevi, E. N. Haran, and B. Ravid. *Chem. Phys. Lett.*, **1**, 475, 1967.

[122] J. M. Hollas. In *Modern spectroscopy*, page 98. John Wiley & Sons, 2004.

[123] Computational Chemistry Comparison and Benchmark DataBase. https://cccbdb.nist.gov/exprot1x.asp.

[124] K. Giles, N. G. Adams, and D. Smith. *J. Phys. B: At. Mol. Opt. Phys.*, **22**, 873, 1989.

[125] M. Gómez-Gallego and M. A. Sierra. *Chem. Rev.*, **111**, 4857, 2011.

[126] F. H. Westheimer. *Chem. Rev.*, **61**, 265, 1961.

[127] L. S. Petralia, A. Tsikritea, J. Loreau, T. P. Softley, and B. R. Heazlewood. *Nat. Commun.*, **11**, 1, 2020.

[128] H. J. Werner et al. Molpro, Version 2015.1, A Package of *ab initio* Program. http://www.molpro.net.

[129] H. J. Werner and P. J. Knowles. *J. Chem. Phys.*, **82**, 5053, 1985.

[130] P. J. Knowles and H. J. Werner. *J. Chem. Phys.*, **89**, 5803, 1988.

[131] J. Loreau, S. Ryabchenko, and N. Vaeck. *J. Phys. B: At. Mol. Opt. Phys.*, **47**, 135204, 2014.

[132] J. Loreau, S. Ryabchenko, J. M. Munoz Burgos, and N. Vaeck. *J. Phys. B: At. Mol. Opt. Phys.*, **51**, 085205, 2018.

[133] C. S. Parmenter. *Faraday Discuss. Chem. Soc.*, **75**, 7, 1983.

[134] T. Uzer and W. H. Miller. *Phys. Rep.*, **199**, 73, 1991.

[135] M. Gruebele and P. G. Wolynes. *Acc. Chem. Res.*, **37**, 261, 2004.

[136] J. E. Gambogi, R. P. L'Esperance, K. K. Lehmann, B. H. Pate, and G. Scoles. *J. Chem. Phys.*, **98**, 1116, 1993.

[137] J. E. Gambogi, K. K. Lehmann, B. H. Pate, G. Scoles, and X. Yang. *J. Chem. Phys.*, **98**, 1748, 1993.

[138] M. A. Suhm, J. T. Farrell Jr, S. H. Ashworth, and D. J. Nesbitt. *J. Chem. Phys.*, **98**, 5985, 1993.

[139] W. Y. Sohn, K-J Cho, S. Y. Lee, S. S. Kang, Y. D. Park, and H. Kang. *Chem. Phys. Lett.*, **525**, 37, 2012.

[140] A. Fernández-Ramos, J. A. Miller, S. J. Klippenstein, and D. G. Truhlar. *Chem. Rev.*, **106**, 4518, 2006.

[141] S. S. Glad and F. Jensen. *J. Am. Chem. Soc.*, **119**, 227, 1997.

[142] J. K. Kim and W. T. Huntress Jr. *Int. J. Mass Spectrom. and Ion Physics*, **16**, 451, 1975.

[143] C. J. Howard, H. W. Rundle, and F. Kaufman. *J. Chem. Phys.*, **53**, 3745, 1970.

[144] S. T. Arnold, R. A. Dressler, M. J. Bastian, J. A. Gardner, and E. Murad. *J. Chem. Phys.*, **102**, 6110, 1995.

[145] T. Stoecklin, D. C. Clary, and A. Palma. *J. Chem. Soc., Faraday Trans.*, **88**, 901, 1992.

[146] M. Wolfsberg, W. A. Van Hook, P. Paneth, and L. P. N. Rebelo. In *Isotope effects: in the chemical, geological, and bio sciences*, page 392. Springer Science & Business Media, 2009.

[147] J. L. Le Garrec, S. Carles, T. Speck, J. B. A. Mitchell, B. R. Rowe, and E. E. Ferguson. *Chem. Phys. Lett.*, **372**, 485, 2003.